Three-Dimensional Cloud-System Modeling of GATE Convection

LEO J. DONNER, CHARLES J. SEMAN, AND RICHARD S. HEMLER

Geophysical Fluid Dynamics Laboratory, NOAA, Princeton University, Princeton, New Jersey

(Manuscript received 3 November 1997, in final form 22 July 1998)

ABSTRACT

Deep convection and its associated mesoscale circulations are modeled using a three-dimensional elastic model with bulk microphysics and interactive radiation for a composite easterly wave from the Global Atmospheric Research Program Atlantic Tropical Experiment. The energy and moisture budgets, large-scale heat sources and moisture sinks, microphysics, and radiation are examined.

The modeled cloud system undergoes a life cycle dominated by deep convection in its early stages, followed by an upper-tropospheric mesoscale circulation. The large-scale heat sources and moisture sinks associated with the convective system agree broadly with diagnoses from field observations. The modeled upper-tropospheric moisture exceeds observed values. Strong radiative cooling at the top of the mesoscale circulation can produce overturning there. Qualitative features of observed changes in large-scale convective available potential energy and convective inhibition are found in the model integrations, although quantitative magnitudes can differ, especially for convective inhibition.

Radiation exerts a strong influence on the microphysical properties of the cloud system. The three-dimensional integrations exhibit considerably less sporadic temporal behavior than corresponding two-dimensional integrations. While the third dimension is less important over timescales longer than the duration of a phase of an easterly wave in the lower and middle troposphere, it enables stronger interactions between radiation and dynamics in the upper-tropospheric mesoscale circulation over a substantial fraction of the life cycle of the convective system.

1. Introduction

Deep convection and its associated mesoscale circulations represent dominant components in the hydrology and radiation of the tropical atmosphere. These cloud systems transport and remove large amounts of water and are thereby important in controlling upper-tropospheric water vapor, which in turn exerts a strong greenhouse effect (Soden and Fu 1995). The spatially extensive, optically thick upper-tropospheric ice clouds in these systems can exert large longwave and shortwave cloud radiative forcing (e.g., Harrison et al. 1990). Thus, these cloud systems are crucial elements in global climate. Significant large-scale heating is associated with these systems, and general circulation models (GCMs) have suggested that modes of large-scale tropical variability depend on the frequency and spatial distribution of deep convection (Slingo et al. 1994). The mass transports associated with these cloud systems lead to redistribution of chemical species and probably play important roles in atmospheric chemistry (e.g., Lelieveld and Crutzen 1994; Stenchikov et al. 1996).

The parameterization of the effects of deep convection in GCMs remains a complex, challenging problem in atmospheric science with many uncertain aspects. The climate in GCMs is sensitive to the details of cumulus parameterization (e.g., Donner et al. 1982; Hack 1994). Most cumulus parameterizations currently used in GCMs have been designed to treat heat and moisture interactions between deep convection and large-scale flows, with little attention to microphysical and radiative aspects or the mesoscale circulations associated with deep convection. Donner (1993) treats mesoscale circulations associated with deep convection but is limited by both current lack of knowledge of the basic processes involved in convective systems and absence of some critical observations of these systems, for example, ice contents in the mesoscale circulations and simultaneous characterization of both the large-scale dynamic environment and microphysical and radiative properties.

High-resolution models that can explicitly resolve individual deep convective elements are a valuable tool for studying the processes associated with these systems and for evaluating cumulus parameterizations for large-scale models. The characteristics of convective cloud systems (including radiation and associated interactions) have been studied with these models (e.g., Tao et al.

Corresponding author address: Dr. Leo J. Donner, Geophysical Fluid Dynamics Laboratory, NOAA, Princeton University, P.O. Box 308, Princeton, NJ 08542.
E-mail: ljd@gfdl.gov

1993; Fu et al. 1995; Chin et al. 1995; Guichard et al. 1996; Grabowski et al. 1996b). They have also been used to evaluate cloud parameterizations (e.g., Gregory and Miller 1989; Xu and Krueger 1991). The equilibrium climates of these models in the absence (Held et al. 1993) and presence (Sui et al. 1994; Grabowski et al. 1996a) of imposed dynamic forcing have been investigated. Until recently, cloud-system models have been two-dimensional, with a few small-domain (several tens of kilometers per side) three-dimensional exceptions (Lipps and Hemler 1986; Redelsperger and Sommeria 1986; Tao and Soong 1986; Dudhia and Moncrieff 1987).

Currently, efforts are underway at several laboratories and universities to study convective systems with larger-domain (several hundreds of kilometers per side) three-dimensional cloud-resolving models. These models have domains significantly larger than those of the individually resolved cumulus elements and are also comparable in size to the resolution of GCMs typically used for climate studies. The purpose of this paper is to examine a three-dimensional large-domain integration of a cloud system for conditions associated with a composite easterly wave from the Global Atmospheric Research Program (GARP) Atlantic Tropical Experiment (GATE). The model is described in section 2. Dynamics and energetics (section 3), microphysics and radiation (section 4), and the role of the third dimension (section 5) are highlighted. In focusing on these issues, the paper aims to evaluate the behavior of the model in a typical case, especially regarding properties that are important for the interaction between convection and larger scales. If models of this nature can capture these features realistically, they have great potential for evaluating cumulus parameterizations and the hypotheses on which parameterizations are based. The results to be presented are generally promising in this regard, although they indicate that some aspects of the models require further development. General questions regarding the basis for parameterization will also require use of models in more synoptic environments than the GATE case considered here.

2. Model description and integration design

The model used for these integrations is a three-dimensional version of that employed by Held et al. (1993). The model uses elastic dynamics, bulk microphysics, and interactive radiation. In addition to adding the third dimension, other modifications include the following. 1) In the bulk aerodynamic formulations for surface sensible- and latent-heat fluxes, atmospheric temperatures and mixing ratios extrapolated to 10-m heights are used. By doing so, observed sensible-heat fluxes (which used atmospheric measurements at 10 m) can be compared more readily with the model. No minimum value is imposed on the horizontal wind speed in the bulk aerodynamic formulation here. 2) An autoconversion threshold for ice of 1.5 g kg^{-1} [instead of zero and similar to the threshold of 1.0 g m^{-3} in Lipps and Hemler (1988)] is used in the bulk microphysics. The model includes two classes of ice: cloud ice and snow. 3) The sponge layer near the model top has a strength $\kappa_0(z - z_0)$. The damping is linear above $z_0 = 13.875$ km with a damping time of 235 s at the model top at 16 km. For potential temperature, the model is damped to observations, instead of the model horizontal means in Held et al. (1993), where the sponge is applied above z_0. The sponge layer is fairly thin, and the model top is only somewhat above the heights to which GATE convection penetrates, following Lipps and Hemler (1986). This offers an obvious advantage in limiting computational demands, but the sponge layer is thinner than in many studies of deep convection (e.g., Held et al. 1993), and active microphysical and radiative processes will be seen to extend through the full vertical extent of the model domain at some times during the integrations. Although some details of the integrations may be artifacts of these limitations, the fundamental character of the modeled convective systems does not appear to have been altered significantly by the use of a fairly thin sponge layer or limited vertical domain.

The horizontal model domain for these integrations is 220 $\times$ 220 km. The horizontal and vertical grid lengths are 2 km and 500 m, respectively. The horizontal domain is similar to that of the GATE B-scale array, from which observations used to force and evaluate the integrations are obtained. It is also typical of resolutions of many climate GCMs in which convective processes are parameterized. A series of test calculations with the model using resolutions from 500 m to 5 km indicated that some basic features of the integrations (e.g., pattern of vertical velocity) began to change noticeably as the resolution was degraded beyond 2 km, motivating the choice of horizontal resolution in the face of the great computational demands of the three-dimensional integrations. Also, note that Golding (1993) successfully modeled intense convection near Darwin (Australia) using 3-km resolution. The model employs periodic lateral boundary conditions. The model time step is 2 s. The model domain moves with the time-dependent, vertically averaged wind, obtained from Thompson et al. (1979). These winds have not been mass weighted, and this movement of the domain will be used only in analyzing the surface precipitation field.

The integrations are performed over a composite easterly wave from GATE. Advantages of this procedure include the presence of well-documented observations and the typical character of the synoptic situation associated with the composite. Disadvantages, relative to integrating for specific cases, arise from the nonlinear relationships between atmospheric structures, forcing, and convection, which limit the extent to which convection arising from composite states in the integration can be compared with composite observations. Another disadvantage is that a diurnal cycle of radiation is not

implemented; instead, radiation calculations are performed with a solar zenith angle of 53°, representing a tropical diurnal average. The radiative-transfer model used here is described in Held et al. (1993).

Large-scale forcing for potential temperature and vapor mixing ratio are imposed as terms added to the thermodynamic and vapor mixing-ratio equations. This large-scale forcing, which depends on height and time, represents the effects of both horizontal and vertical large-scale advection of temperature and vapor mixing ratio. Feedbacks by convection on the easterly wave and its large-scale forcing (Paradis et al. 1995) are excluded by this procedure. Height-dependent observations from GATE (Thompson et al. 1979) for temperature, mixing ratio, apparent heat source, apparent moisture sink, and duration of GATE wave phases are used. The large-scale forcings (representing total advection) for potential temperature $\partial_{\rm LS}\overline{\theta}$ and mixing ratio $\partial_{\rm LS}\overline{q}$ are given by

$$\partial_{LS}\overline{\theta} = \frac{\partial\overline{\theta}}{\partial t} - \frac{Q_1\pi}{c_p}, \tag{1}$$

$$\partial_{LS}\overline{q} = \frac{\partial\overline{q}}{\partial t} + \frac{Q_2}{L_1}. \tag{2}$$

Potential temperature is denoted by θ, vapor mixing ratio by q, specific heat capacity at constant pressure by c_p, and latent heat of vaporization by L_1. The reciprocal Exner function π is $(p_0/\overline{p})^{R_d/c_p}$, where p is pressure, p_0 is a reference pressure (100 hPa), and R_d is the gas constant for dry air. The apparent heat source Q_1 is given by

$$Q_1 = \frac{\partial\overline{s}}{\partial t} + \overline{\mathbf{v}}\cdot\nabla(\overline{s}) + \frac{\partial}{\partial p}(\overline{\omega}\,\overline{s}), \tag{3}$$

where $s = c_pT + gz$ is the dry static energy, $\mathbf{v}$ is the horizontal velocity vector, and ω is the (pressure) vertical velocity (T and g denote temperature and the gravity constant, respectively). A large-scale average is indicated by an overbar. The apparent moisture sink Q_2 is given by

$$Q_2 = -L_1\left[\frac{\partial\overline{q}}{\partial t} + \overline{\mathbf{v}}\cdot\nabla(\overline{q}) + \frac{\partial}{\partial p}(\overline{\omega}\,\overline{q})\right]. \tag{4}$$

The model integrations are initialized with height-dependent temperature and mixing-ratio soundings from GATE phase 1 in Thompson et al. (1979). Perturbations are imposed on the initial mixing ratio to initiate convection. The perturbations vary in the horizontal but are constant throughout the lowest 1.5 km in each column of the model. The perturbations are horizontally random, generated from a uniform distribution between ± 2 g kg^{-1}. These perturbations are similar to those employed by Lipps and Hemler (1986). The perturbations are chosen to be random so as not to impose organized structure on the convection when it develops, and Lipps and Hemler (1986) found that perturbations of this magnitude were sufficient to initiate convection. However, further research as to the most appropriate magnitude and structure of these initial perturbations is warranted. The integrations extend from phase 1 through phase 7 of GATE. (Phase numbers refer to particular synoptic features of the composite easterly wave. For example, phase 4 refers to the trough and phase 8, to the ridge, while phases 2 and 6 indicate maximum north and south winds, respectively. Intermediate numbers indicate intermediate synoptic phases.) Phase 8, with little observed deep convection, is not used in the integration. Phase 1, also with limited deep convection, is used in the integration to allow the model to spin up. Using Table 1 of Thompson et al. (1979), the durations of phases 1–7 are taken as 10, 14, 9, 10, 8, 13, and 9 h, respectively. The local tendencies of potential temperature and mixing ratio in (1) and (2) are evaluated by differencing the potential temperatures and mixing ratios at the beginning of each wave phase in Thompson et al. (1979) and dividing by the duration of the wave phase. Apparent heat sources and moisture sinks are interpolated linearly between their Thompson et al. (1979) values at the beginning of each wave phase. Zonal and meridional velocity components are interpolated from Thompson et al. (1979) to hourly frequency; these values are used to update the base-state velocity each hour. This approach differs from that used, for example, by Grabowski et al. (1996b), who relax the base-state wind toward imposed large-scale winds. No difficulties have been noted with the direct imposition of observed wind profiles at hourly frequency in the present integrations.

Time-dependent surface temperatures are imposed. These temperatures yield the surface sensible-heat fluxes in Thompson et al. (1979), when their formulations for heat flux and temperature profiles are used.

Three integrations are considered. The three-dimensional integration is referred to as ''3D.'' To evaluate the effect of the third dimension, a parallel two-dimensional integration (''2D'') is performed. The 2D integration uses only zonal-wind components and is confined to a height–longitude plane with no meridional dimension. In both 3D and 2D, radiative heating and cooling are large relative to other diabatic and dynamic processes. The effect of radiation is isolated by performing a third integration, ''2D No Radiation,'' which is identical to 2D but with no solar or longwave radiation.

Large-scale potential-temperature forcing $\partial_{\rm LS}\overline{\theta}$ is shown in Fig. 1a. Large-scale forcing destabilizes the lower and middle troposphere appreciably from about 25 to 45 h, the transition from maximum low-level north winds through the trough axis in the easterly wave. The upper troposphere is stabilized as low-level southerly flow is established in advance of the approach of the ridge axis. The magnitude of this stabilization is less than the magnitude of the destabilization of the lower and middle troposphere during the earlier stages of the easterly wave. Figure 1b shows the large-scale moisture

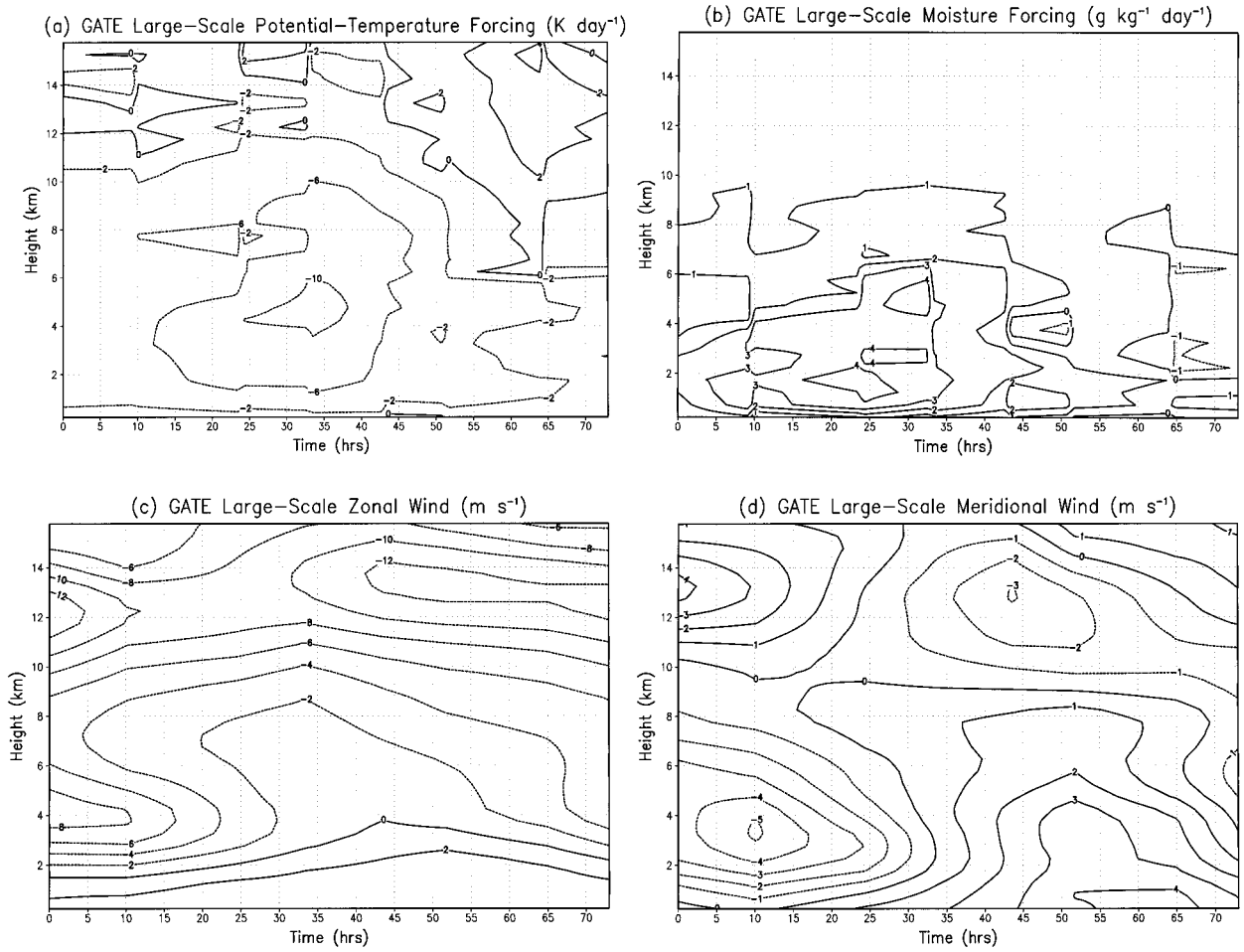

FIG. 1. Imposed large-scale tendencies for (a) potential temperature and (b) vapor mixing ratio. Imposed large-scale (c) zonal and (d) meridional wind.

forcing $\partial_{LS}\overline{q}$. The largest moistening occurs some hours before the lower troposphere is most rapidly destabilized thermally, and drying (of smaller magnitude) occurs in the lower troposphere as the ridge approaches. Figures 1c and 1d show the horizontal velocity components (relative to the earth). Easterly flow (except in the lower troposphere) and easterly shear prevail, and shear is strongest after the low level has been most intensely destabilized.

3. Dynamics and energetics

The motion fields associated with the convective cloud system are quite complex and exhibit several forms of organization. Figures 2a and 2b illustrate some examples, just after the onset of vigorous deep convection (11.25 h into the integration). Vertical organization from 2D is shown in Fig. 2a. (Unless otherwise noted, all figures depict the model domain as it moves with the vertical average of the base-state flow.) Convective cores have vertical extents as great as 8 km. Weak downdrafts occur adjacent to and below the updrafts in regions of strong evaporative cooling, where rain has been shed from the cores. A dynamically active mesoscale pattern characterizes the region downstream of the most developed convective core. (Note in Fig. 1c that zonal winds from 10 to 12 h at 8–10 km are easterly between 2 and 6 m s^{-1}, while they are easterly between 6 and 8 m s^{-1} between about 3 and 5 km. The convective cores at heights less than 8 km evidently move more rapidly to the east than does the material detrained at their tops.) Averaged over the preceding 11.25 h, this dynamically active region is where the most intense gradients in destabilizing radiation occur, with heating at the base of this region of detrained condensate around 8–9 km and cooling at its top, around 11–12 km (discussed in detail in section 4). The small-scale updrafts and downdrafts in this anvil circulation transport heat upward from its base, opposing the pattern of destabilizing radiation. Figure 2b displays horizontal organization from 3D at 11.25 h into the integration on a level 9.5 km above the ground. Several concentrated cores have vertical velocities exceeding 10 m s^{-1}. The maximum vertical velocity reaches nearly 18 m s^{-1}. Figure

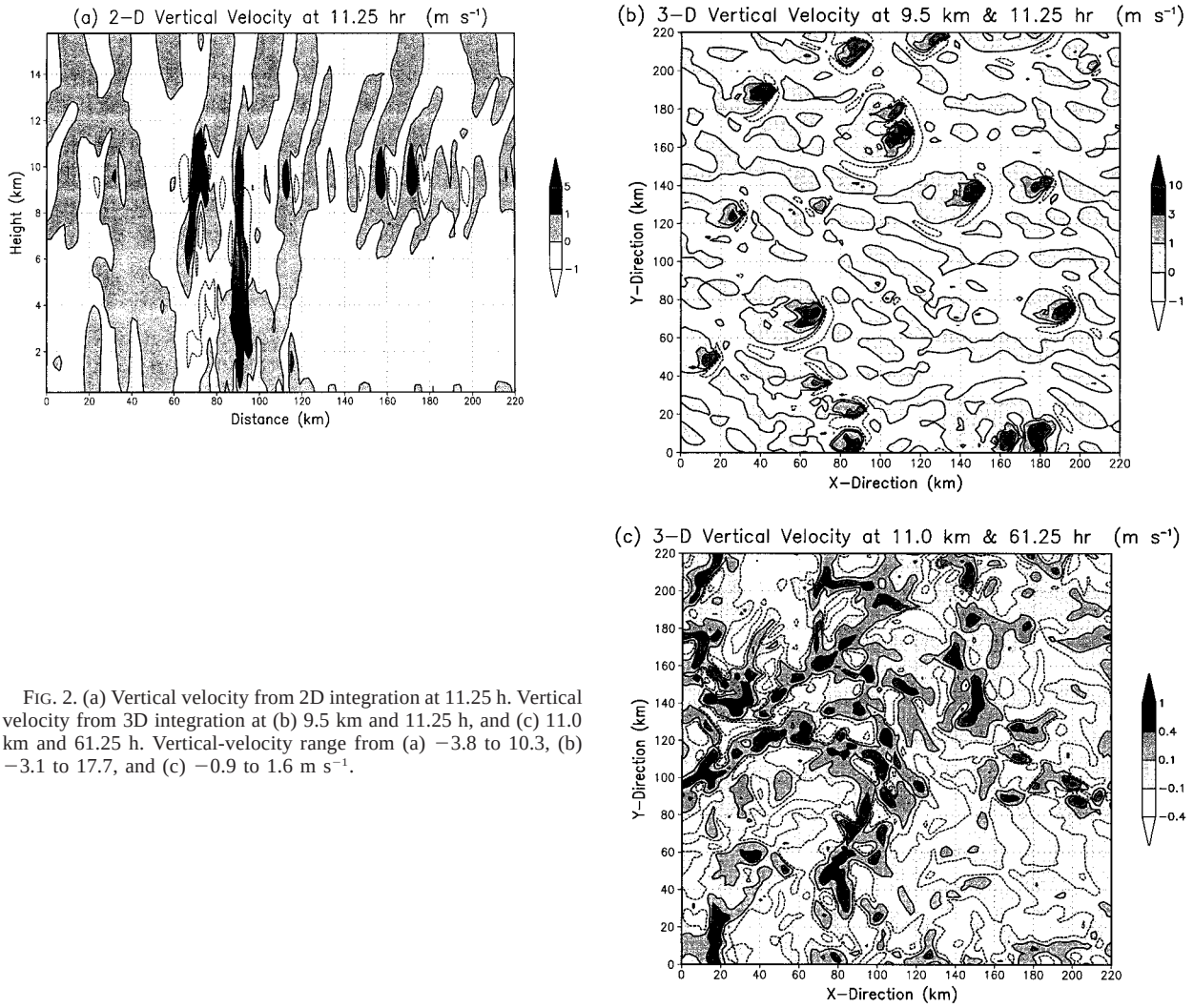

FIG. 2. (a) Vertical velocity from 2D integration at 11.25 h. Vertical velocity from 3D integration at (b) 9.5 km and 11.25 h, and (c) 11.0 km and 61.25 h. Vertical-velocity range from (a) −3.8 to 10.3, (b) −3.1 to 17.7, and (c) −0.9 to 1.6 m s^{-1}.

2c shows the 3D pattern much later in the life cycle of the convective system at 11.0 km. The level depicted is in the mesoscale stratiform portion of the convective system and is characterized by many elongated areas of upward and downward motion of modest magnitude. As will be discussed in more detail in section 4, the mesoscale stratiform area is strongly destabilized by radiation. Small-scale convective motions in the stratiform anvil act to transport heat so as to partially compensate for this destabilizing radiation. In addition, gravity waves may be propagating through the anvil; animation of the integration solutions shows stronger evidence of gravity waves in the anvil during earlier stages of the integration when deep convective towers are also present.

Very little observational information is available on the small-scale structure of fields such as those discussed above. However, some indications are evident in the distributions of boundary layer relative humidity measured at a horizontal resolution of approximately 25 m over a domain of 100 km off the coast of Florida. The frequency distributions of these measured humidities and those produced by the cloud-system model can be roughly rationalized (Haywood et al. 1997). Although many factors limit the extent to which the observed and model humidities can be compared in that study, it is an encouraging finding regarding the model's ability to capture the statistical character of the small-scale distribution.

Figure 3 depicts the principal terms in the energy balance, averaged over the model's horizontal domain. The convective system produces its first deep convection about 10 h after large-scale forcing acts on the random humidity perturbation in the boundary layer, as can be seen from the condensation pattern in Fig. 3a. Lipps and Hemler (1986) note that an appreciable time is required before convection develops with this model with the imposed initial perturbations. It is unclear what factors are responsible; the random organization of the initial perturbations and the inability of the model to

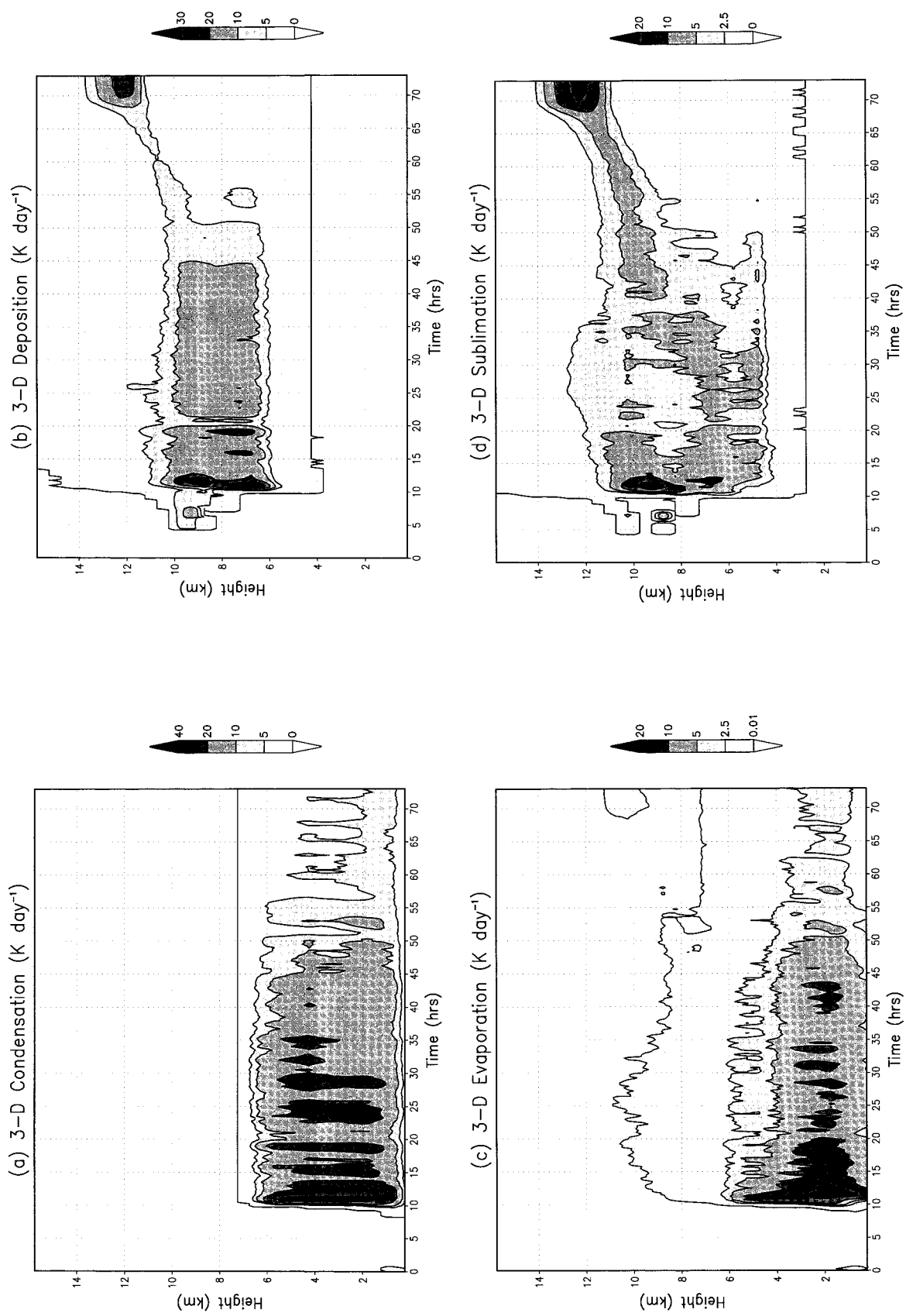

FIG. 3. The 3D horizontally averaged (a) condensation, (b) deposition, (c) evaporation, (d) sublimation, (e) freezing, (f) melting, (g) potential-temperature flux $\overline{\rho c_p w'\theta'}$, and (h) vapor flux $\overline{\rho w'q'}$. Flux range from (g) −25 to 228 W m^{-2} and (h) −0.003 to 0.207 g m^{-2} s^{-1}.

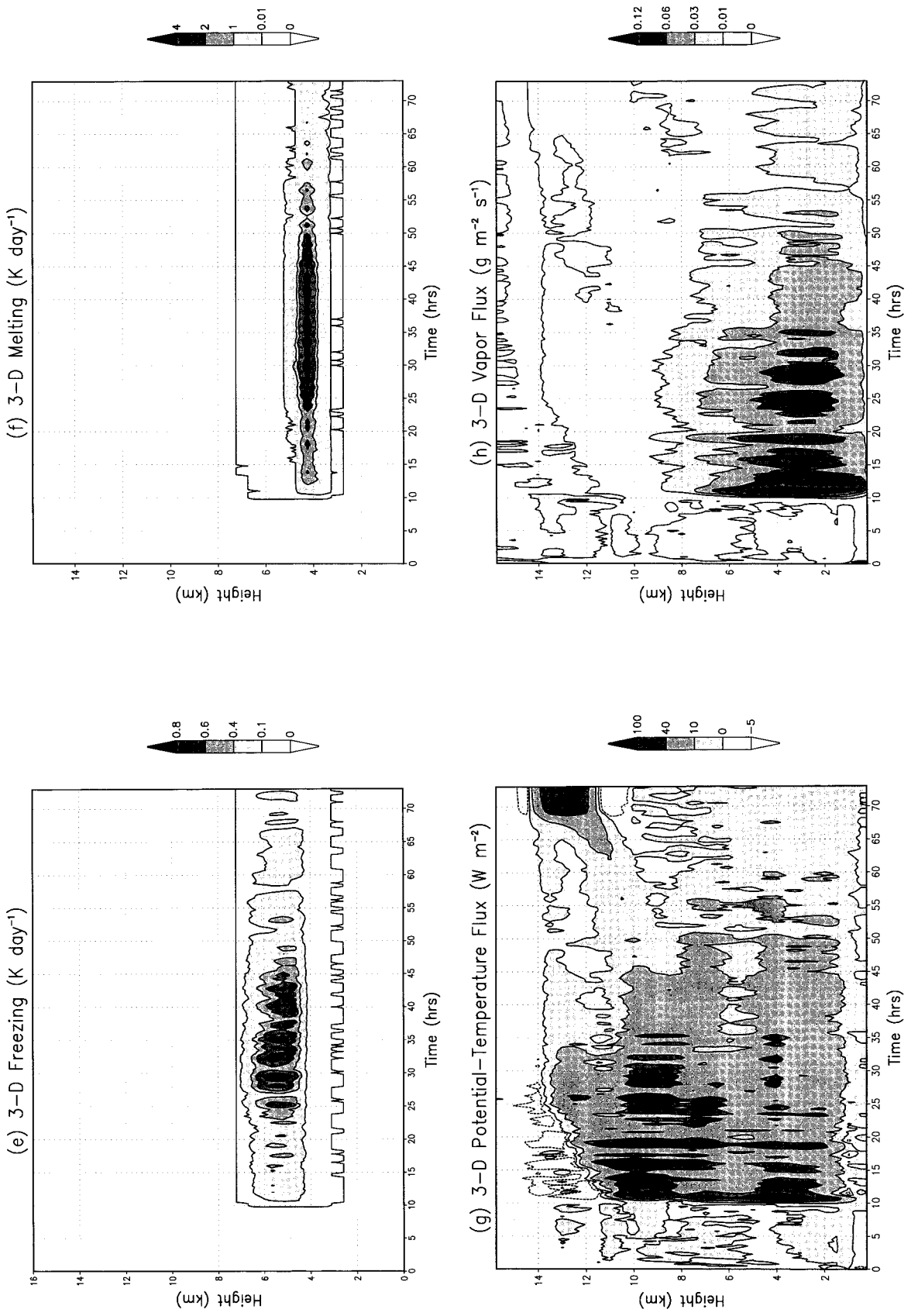

FIG. 3 (*Continued*)

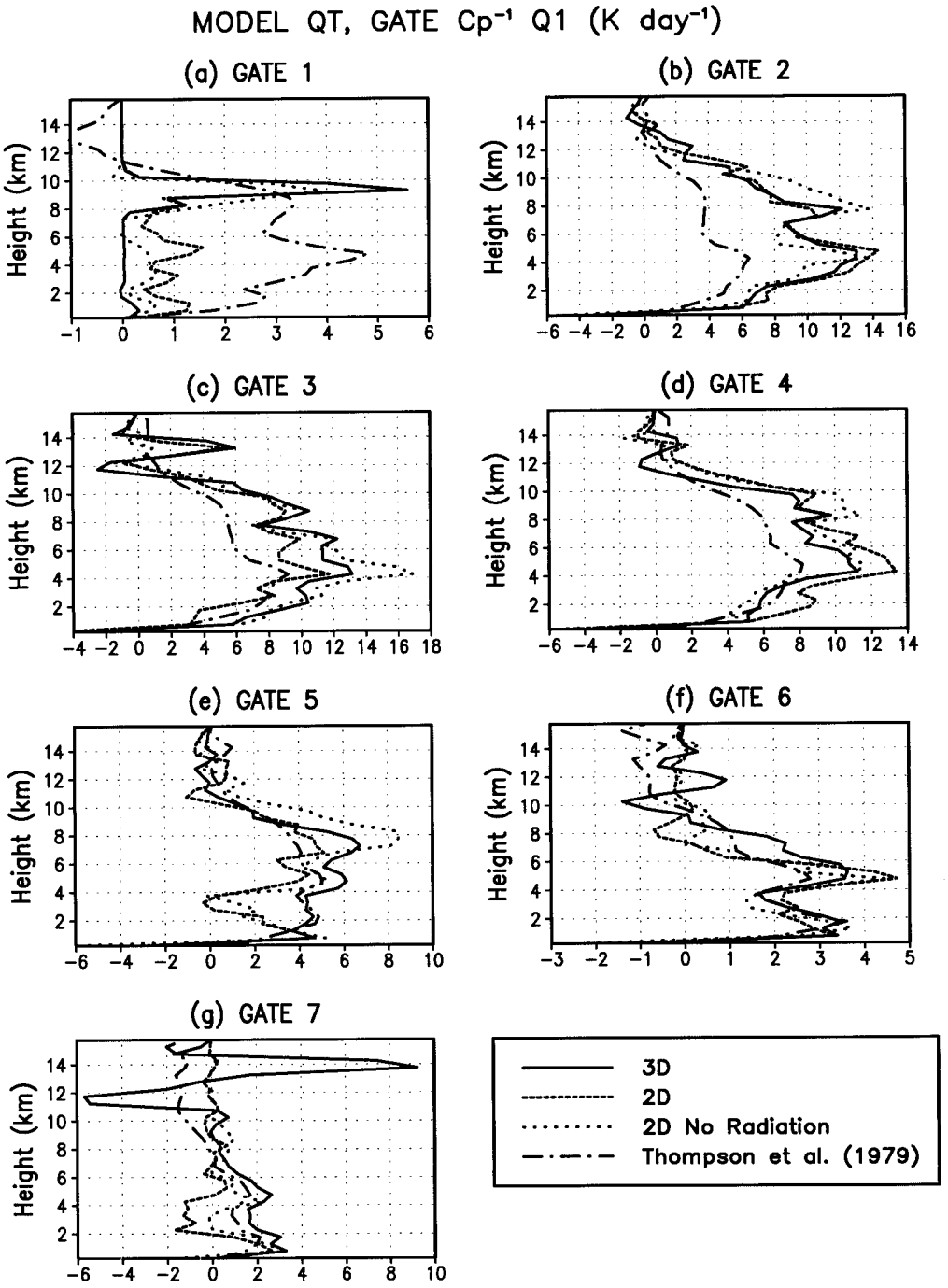

FIG. 4. (a)–(g) Phase-averaged Q_T from model integrations and Q_1/c_p from GATE observations; (h)–(n) phase-averaged Q_Q from model integrations and Q_2/L_1 from GATE observations.

resolve smaller-scale, incipient circulations that may precede deep convection are possibilities. A particularly vigorous burst of deep condensation occurs at the earliest stages of the system. For the following 20 h or so, condensation of somewhat intermittent character remains pronounced in deep towers. Condensation gradually dissipates thereafter. (The microphysics formulation allows no cloud ice below −12°C, a fairly crude approximation resulting from the use of a combined, single variable for cloud liquid and cloud ice. The observed and modeled temperatures fall below this value between 7 and 7.5 km, explaining the time-independent zero line for condensation in Fig. 3a.) Deposition (Fig. 3b) is generally a vertical extension of condensation,

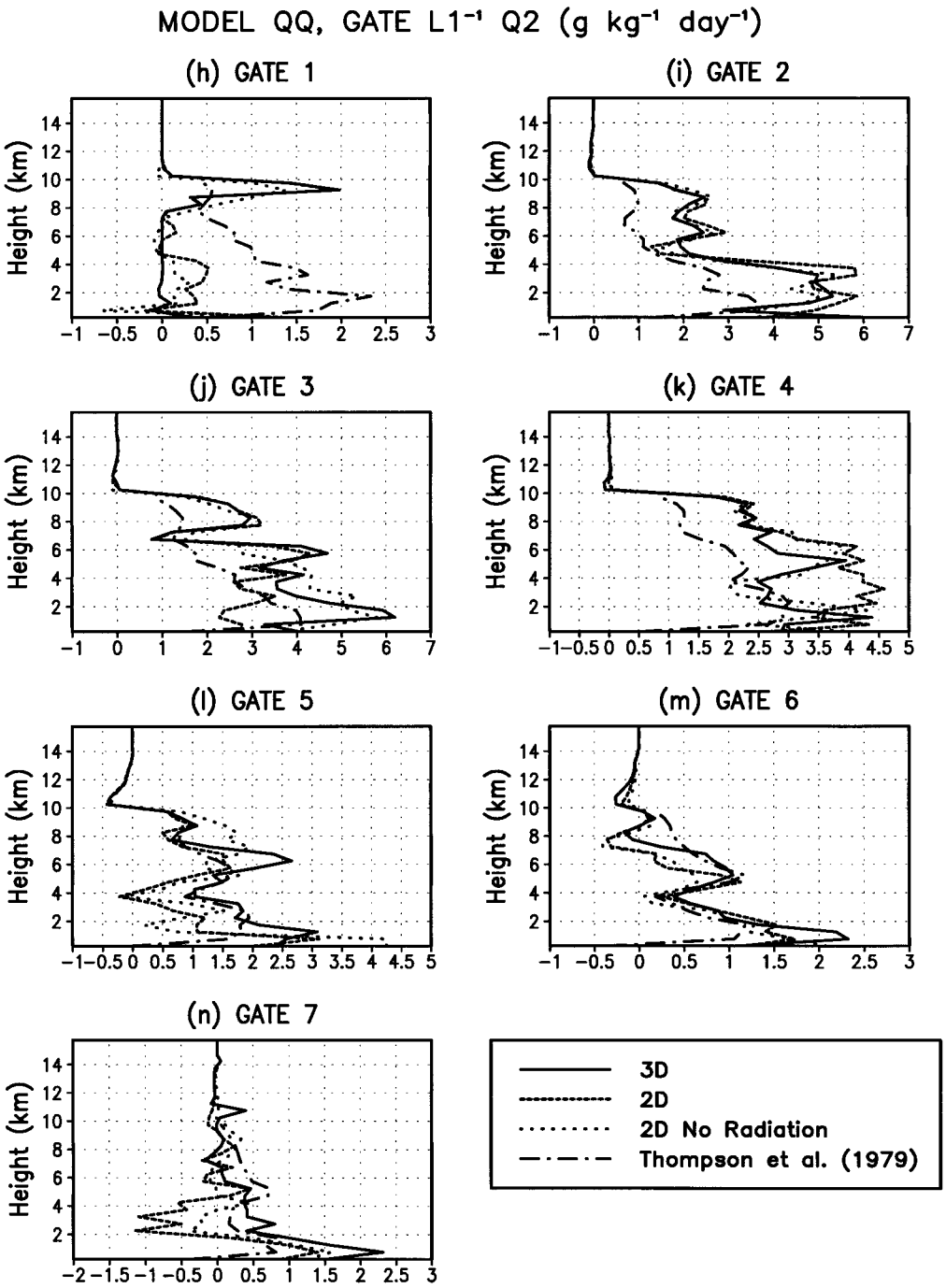

FIG. 4. (*Continued*)

except that a maximum appears around 12 km near the end of the integration. This deposition is associated with overturning motions in the stratiform anvil, which has been destabilized by radiation (Fig. 2c) and has no direct connection to the deep convective towers that dominate the early stages of the integration. Evaporation of cloud liquid and rain (Fig. 3c) is generally concentrated at lower heights than condensation. Evaporation maxima often occur nearly simultaneously with condensation maxima. Sublimation (Fig. 3d) also exhibits a tendency to match its maxima with those of deposition. Freezing (Fig. 3e) is of much smaller magnitude than the foregoing processes. Its maxima occur during the stages of the system still dominated by deep convective towers but are delayed appreciably; condensate builds up before the onset of appreciable freezing. Both sublimation and

freezing persist slightly where temperatures are somewhat above 0°, a result of the presence of snow falling from colder areas. The conversion of snow to vapor (before it melts) in these warm areas is sublimation. When snow accretes cloud liquid in these warm areas, freezing of the cloud liquid occurs. Considerations similar to those for freezing also apply for melting (Fig. 3f), except that it is concentrated in a thinner layer where it is locally of greater magnitude than freezing. In addition to phase changes, significant fluxes of heat and moisture are produced by the motions in the convective system. The potential temperature flux $c_p\overline{\rho w'\theta'}$ (Fig. 3g) exhibits maxima around 4 km in deep convective towers and also around 10 km. Examination of profiles of vertical velocity (not shown) indicates that large upward vertical velocities around 10 km occur in individual convective towers. There are also smaller-scale updrafts and downdrafts in the mesoscale stratiform region. Both convective-scale and stratiform vertical motions can contribute to the heat flux. Toward the end of the integration, small-scale, shallow convection in the radiatively destabilized anvil produces moderate heat fluxes. Convergence (divergence) of these heat fluxes opposes radiative cooling (heating) in the anvil; radiation in this cloud system will be discussed in section 4. Water vapor fluxes (Fig. 3h) are broadly in phase with lower-troposphere heat fluxes. (Temperatures are too cold for appreciable vapor fluxes where strong upper-troposphere heat fluxes develop.) The lower-troposphere water vapor fluxes provide a strong signal of deep convection in the first half of the integration.

The aggregate effects of phase changes and convergence of fluxes act to force the temperature and water-vapor fields of large-scale flows in which convective systems develop. Cumulus parameterizations for large-scale models attempt to infer these forcings from the properties of large-scale flows. The ability of cloud-system models to match large-scale heat sources and moisture sinks diagnosed from observations provides a measure of their skill in representing processes that are important in the interaction between cloud systems and large-scale flows. The usefulness of cloud-system models in evaluating and developing cumulus parameterizations obviously depends on the ability of these models to represent these interactions.

Figures 4a–g illustrate the sums of heating by phase changes and flux convergence for the cloud-system model integrations, defined as

$$Q_T = \frac{\sum_{i=1}^{6} L_i \overline{\gamma_i}}{c_p} - \frac{1}{\overline{\rho}\,\pi}\frac{\partial}{\partial z}\left(\overline{\rho}\overline{w'\theta'}\right), \qquad (5)$$

where γ_i is the rate of the ith phase transformation, w is vertical velocity, and ρ is density. The subscripts i run from 1 to 6 and refer to condensation, evaporation, deposition, sublimation, freezing, and melting, respectively. The latent heats of vaporization, sublimation, and fusion are indicated by L_1, L_3, and L_5, respectively. (The model has one set of levels for w and another set of levels for θ. Vertical derivatives of fluxes are obtained by first interpolating θ to the w levels and evaluating the fluxes on those levels. The derivatives are then vertical finite differences centered at the θ levels. An analogous procedure is employed to evaluate moisture fluxes.) All phase changes are defined as positive semidefinite, so

$$L_2 = -L_1, \qquad L_4 = -L_3, \qquad L_6 = -L_5.$$

Overbars refer to averages over the horizontal domain of the model, and primes refer to departures therefrom. Also illustrated in Figs. 4a–g are related quantities diagnosed from observations by Thompson et al. (1979), Q_1/c_p, following the definition [(3)]. Note that Q_T does not include radiation, which, along with subgrid diffusion (including convergence of surface heat flux), would render Q_T and Q_1/c_p consistent. Radiation has been omitted from Q_T to focus on the effects of phase changes and flux convergence. With a few exceptions, the magnitude of radiative heating and cooling between 1 and 6 km is less than 2 K day^{-1}. As will be discussed in section 4, radiative effects are much greater above 6 km, where their addition to Q_T produces appreciable changes in the total large-scale forcing by the convective system relative to the profiles in Figs. 4a–g.

Once convection begins, the sum of the model phase changes and flux convergence generally captures successfully key features in the shapes of the profiles of the apparent heat source below approximately 7 km. The temporal evolution of the amplitude of the model heat source differs from the evolution of the model heating through the trough, with the model amplitude too small initially and then too large. This may be a result of the procedure used to initiate the convection, which starts later in the model than in the observations. As will be discussed shortly, the delayed onset of deep convection allows more convective available potential energy to build up than is observed, so, once convection is established, it is more vigorous than observed. By the trough exit (phase 5), the magnitudes of the model and diagnosed apparent heat sources are comparable in the lower and middle troposphere. Above 7 km or so, Q_T exhibits more vertical structure than the diagnosed heat sources. Comparing the modeled heating from phase changes and flux convergence in Fig. 4 directly with the diagnosed heat source is not very meaningful at these heights, since radiative heating and cooling, themselves having characteristic vertical structures, become large in magnitude relative to the phase changes and flux convergence. Especially in the later stages of the integration, differences between 3D and the other integrations emerge in the upper troposphere. These differences will be discussed in more detail later and are of particular interest in the context of the effects of radiation, which heat the lower portions of the meso-

scale stratiform circulation (at approximately 10 km) and cool its upper portions (at approximately 14 km).

Figures 4h–n show the sums of moisture sinks by phase changes and moisture-flux convergence for the cloud-system model. These sums Q_Q are defined as

$$Q_Q = \sum_{i=1}^{4} \frac{|L_i|}{L_i}\overline{\gamma_i} + \frac{1}{\overline{\rho}}\frac{\partial}{\partial z}\left(\overline{\rho}\,\overline{w'q'}\right). \quad (6)$$

(As with Q_T, subgrid diffusion is not included in Q_Q, which is defined to be a measure of the direct moisture sink produced by the resolved effects of convection on domain-scale flows.) The corresponding quantities diagnosed from observations by Thompson et al. (1979), Q_2/L_1, are also shown. Since the moisture budget lacks a radiative component, Q_Q and Q_2 are more directly comparable. As was also the case for the heat budget, the modeled moisture sink is too weak during phase 1 and then too strong in phase 2, when the initial stages of convection are stronger than observed. In phases 5–7, the modeled moisture sinks agree reasonably in broad features with observations, especially for 3D; an exception is 2D in phase 7 from 2–4 km, where Q_Q is appreciably less than Q_2/L_1. Another exception is near the surface, where the effects of the modeled surface moisture flux are not included in Q_Q; analogous observed effects are included in Q_2. The convergence of modeled surface moisture fluxes in the lowest layer produces vapor tendencies of about 3–9 g kg^{-1} day^{-1} and would generally decrease Q_Q values at least to those of Q_2/L_1. (Similar behavior characterizes the heating in Figs. 4a–g, where convergence of surface fluxes not included in Q_T would add around 1–4 K day^{-1} near the surface, bringing these values closer to diagnosed Q_1/c_p there.) The Q_2 and Q_Q profiles both exhibit maxima in the lower troposphere; both also are fairly consistent in showing a secondary maximum in the middle troposphere during some of the phases.

Figures 5a–g show the evolution of the domain-averaged temperature, relative to observations. In the lower troposphere, the differences between the modeled and observed temperatures show a relatively small cool bias in the model. Above 7 km, effects of radiation and dimensionality are apparent. Particularly evident toward the end of the integration is the effect of radiative heating of the base of the mesoscale stratiform circulation, which produces warmer temperatures in the model than in the observations from about 7 to 14 km. The magnitude of the temperature differences is similar to that obtained by Grabowski et al. (1996b) in their two-dimensional model, although the patterns differ, with the latter obtaining temperatures about 5 K colder than observed above 16 km toward the end of their integration. (Recall that the present integration damps to observed temperatures above about 14 km.)

Relative to observations, the model mixing ratios are generally somewhat high, although the 3D integration is drier than the others below 4–5 km after the trough axis (Figs. 5h–n). Grabowski et al. (1996b) find that the largest moist biases in their integrations are around 1 g kg^{-1} at heights of 6 km, a somewhat higher height than here in most cases. The relative humidity (with respect to liquid, Figs. 5o–u) is too high in the model, especially in the stratiform region. This pattern is also obtained by Grabowski et al. (1996b); their maximum bias is around 30%. The model and observed fields integrated over phases 1–7 (with weighting corresponding to the observed composite lengths of these phases) are shown in Fig. 6. Model temperatures are slightly cooler than observed below approximately 12 km in the two-dimensional calculations and below approximately 7 km in the three-dimensional calculations. Between 7 and 12 km, the three-dimensional calculations are warmer than observed (Figs. 6a,b). Consistent with the individual phases, the model is too moist through much of middle and upper troposphere (Figs. 6c–f). The sharp reduction in the observed relative humidity around 6 km does not occur in the model, as also seen in Grabowski et al. (1996b). Lateral periodic boundary conditions and uncertainties in ice removal by sedimentation could be responsible, but note also that upper-tropospheric humidity is difficult to measure.

Simple, conceptual models of deep convection often relate intensity to convective available potential energy (CAPE), and cumulus parameterizations often are cast in terms of quantities related to CAPE (Emanuel 1994, chap. 6; Arakawa and Schubert 1974; Fritsch and Chappell 1980). [CAPE is defined here as the energy released by a parcel between the level of free convection and the level of zero buoyancy, as in Donner (1996).] Modeled and observed CAPE are displayed in Fig. 7a. (Model CAPE calculations initiate parcel ascent at the surface, and observations at 1000 hPa. CAPE values are sensitive to the level from which the parcel is assumed to ascend. Observations are available and plotted as averages over each phase.) Prior to the onset of convection in the model, CAPE builds up to values appreciably greater than observed. This buildup is a result of the continuing action of large-scale forcing as convection fails to develop; the onset of convection is evidently delayed in the model relative to the atmosphere. Once convection begins, CAPE is consumed very rapidly. Observed CAPE values also decline through the convectively dominated stages of the integration, although not nearly so dramatically. From about 25 h onward, observed CAPE values change only slightly. Two-dimensional and observed CAPE values tend upward toward the end of the period, albeit later in the model than in observations, with model CAPE generally somewhat less than observed. The development of large CAPE before convective onset in the model is consistent with the Q_T pattern in Fig. 4, with model values too low prior to convection and too large in the early stage of convection. If cloud-system models are to be used to evaluate closure hypotheses for cumulus parameterization, significant attention must be given to the realism of

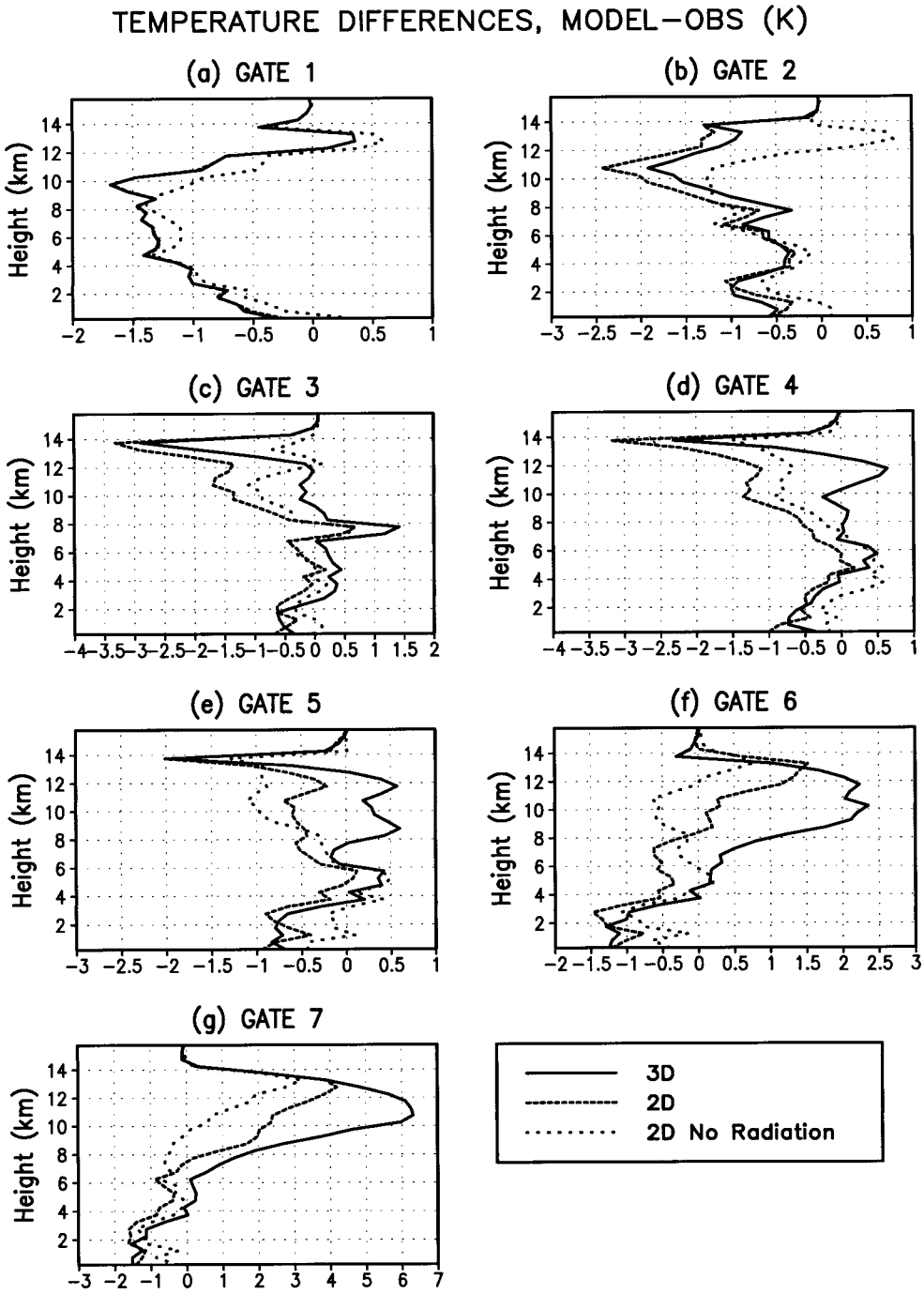

FIG. 5. Phase-averaged (a)–(g) temperature differences, (h)–(n) vapor mixing-ratio differences, and (o)–(u) relative-humidity (liquid) differences between GATE observations and model integrations.

model CAPE evolution. CAPE during early stages may depend on the procedure used to initiate convection. Later stages show reasonable agreement in CAPE.

In addition to CAPE, convective inhibition (CIN) is likely to be an important control on convection. CIN is the energy required for a parcel to reach its level of free convection. If a mechanism to provide energy sufficient to overcome CIN is not available, convection may not occur, regardless of the amount of CAPE. Some cumulus parameterizations (e.g., Kuo 1974) include criteria requiring that this energy be supplied by the large-scale flow before deep convection can occur. Observed and model CIN values are shown in Fig. 7b. There is variability among the different model CIN evolutions.

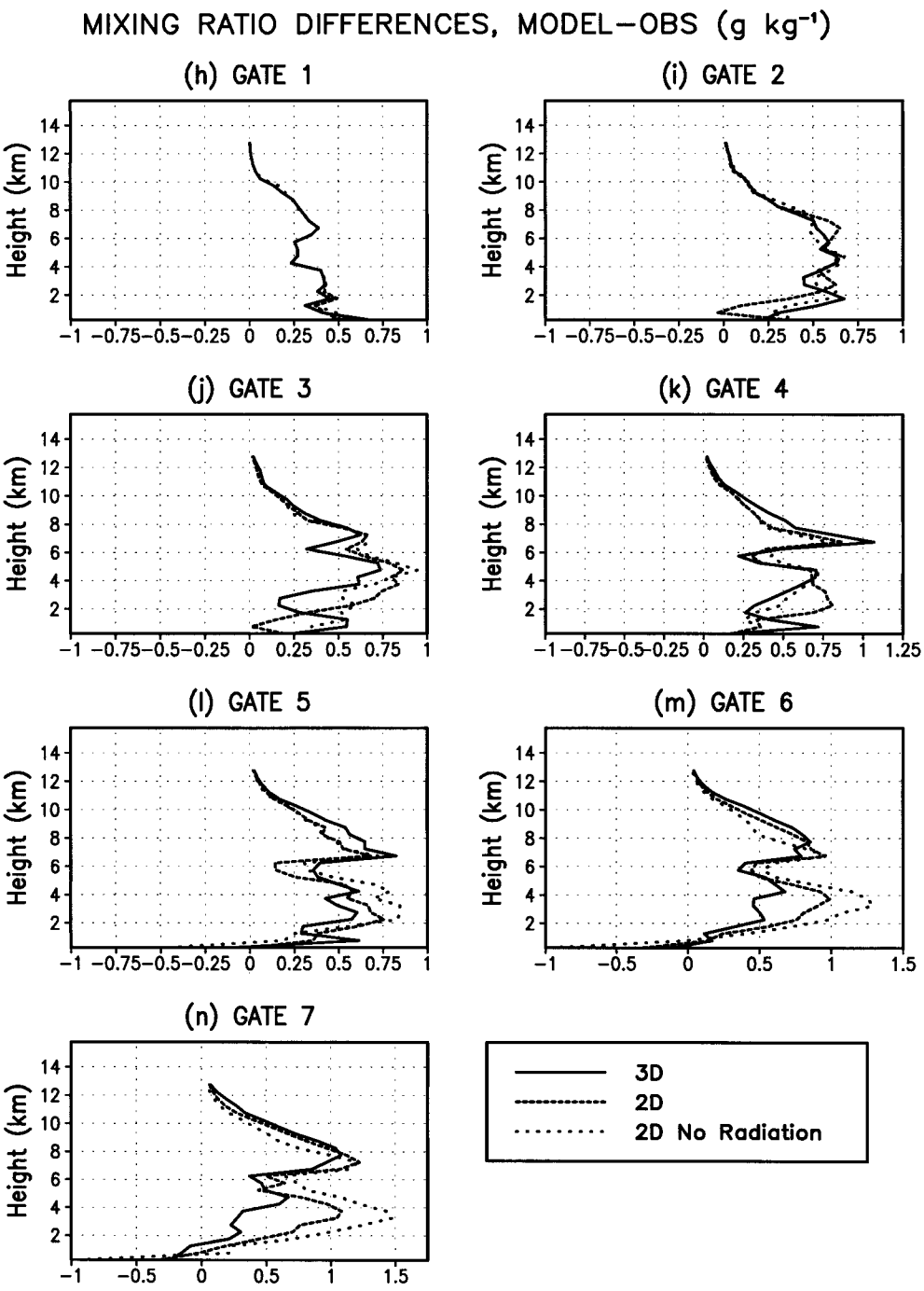

FIG. 5. (*Continued*)

There is a rough tendency for CIN to increase in both the model and observations as the stages dominated by deep convection progress and for CIN to decrease toward the end of the integration. Model CIN drops dramatically before convection begins. The model requires that much less CIN exist before convection occurs than is observed, at least with the initialization used here. The general sequence revealed by Fig. 7 is CAPE buildup and CIN reduction by large-scale processes prior to the onset of convection. Once convection begins, CAPE is consumed and CIN again increases. After approximately 30 h, the convective system changes to a regime dominated by the mesoscale stratiform circulation (cf. Fig. 3). During the mesoscale regime, CAPE declines

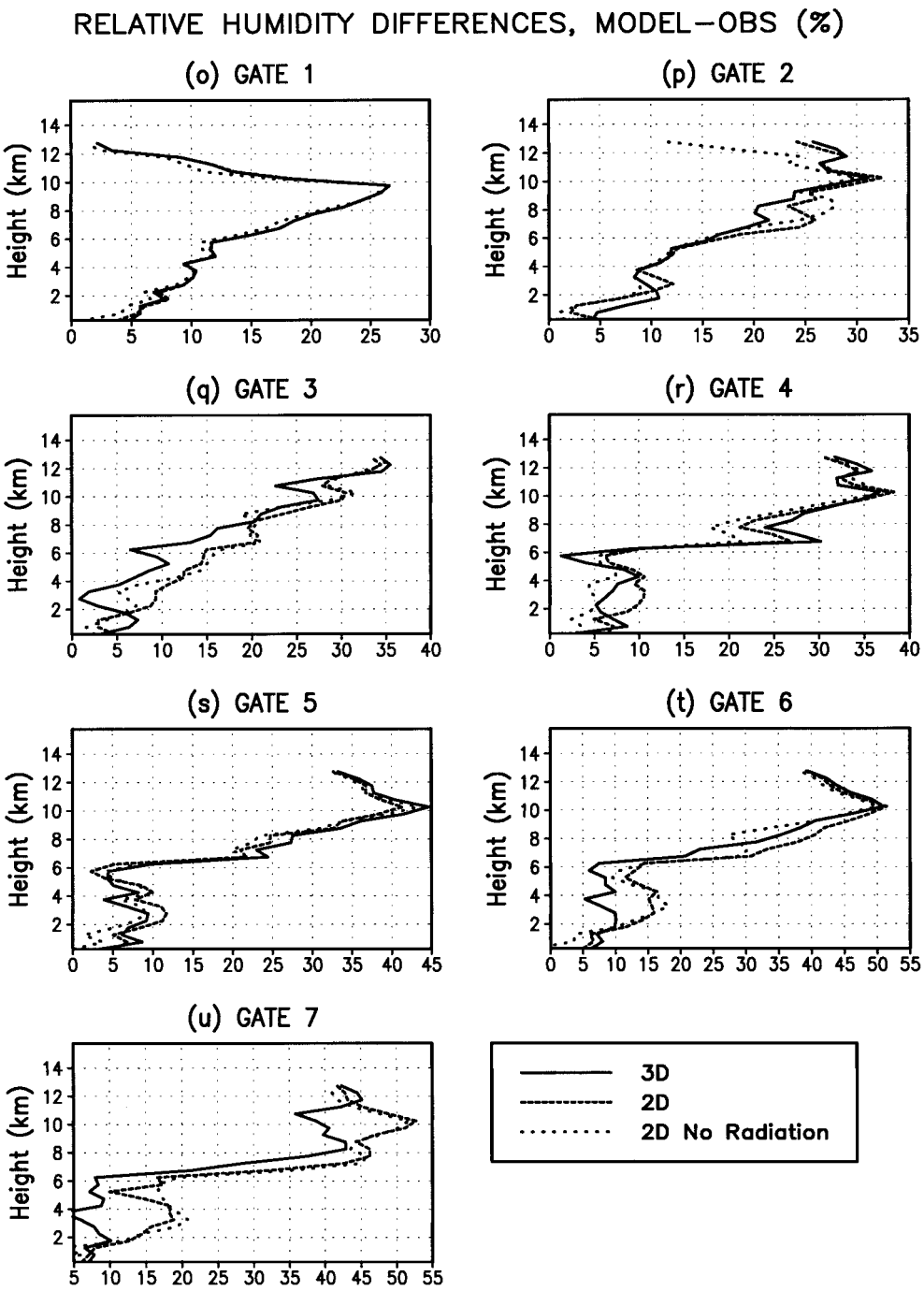

FIG. 5. (*Continued*)

only gradually, presumably as a result of weaker stabilization as convection becomes less dominant. CIN also declines later during this period.

Figure 7 illustrates large-scale averages of CAPE and CIN. Large-scale observations and models enable evaluation at these scales. However, there can be large variations in these fields at smaller scales. To the extent that the concept of parcels is valid in considering convective motions, parcels will ''feel'' CAPE and CIN on small scales. Figure 8 shows that variations in CAPE occur below the large scale, a result that challenges the ways in which large-scale CAPE and CIN apply as controls on the occurrence and intensity of convection. The realism of the statistical distributions of CAPE and CIN

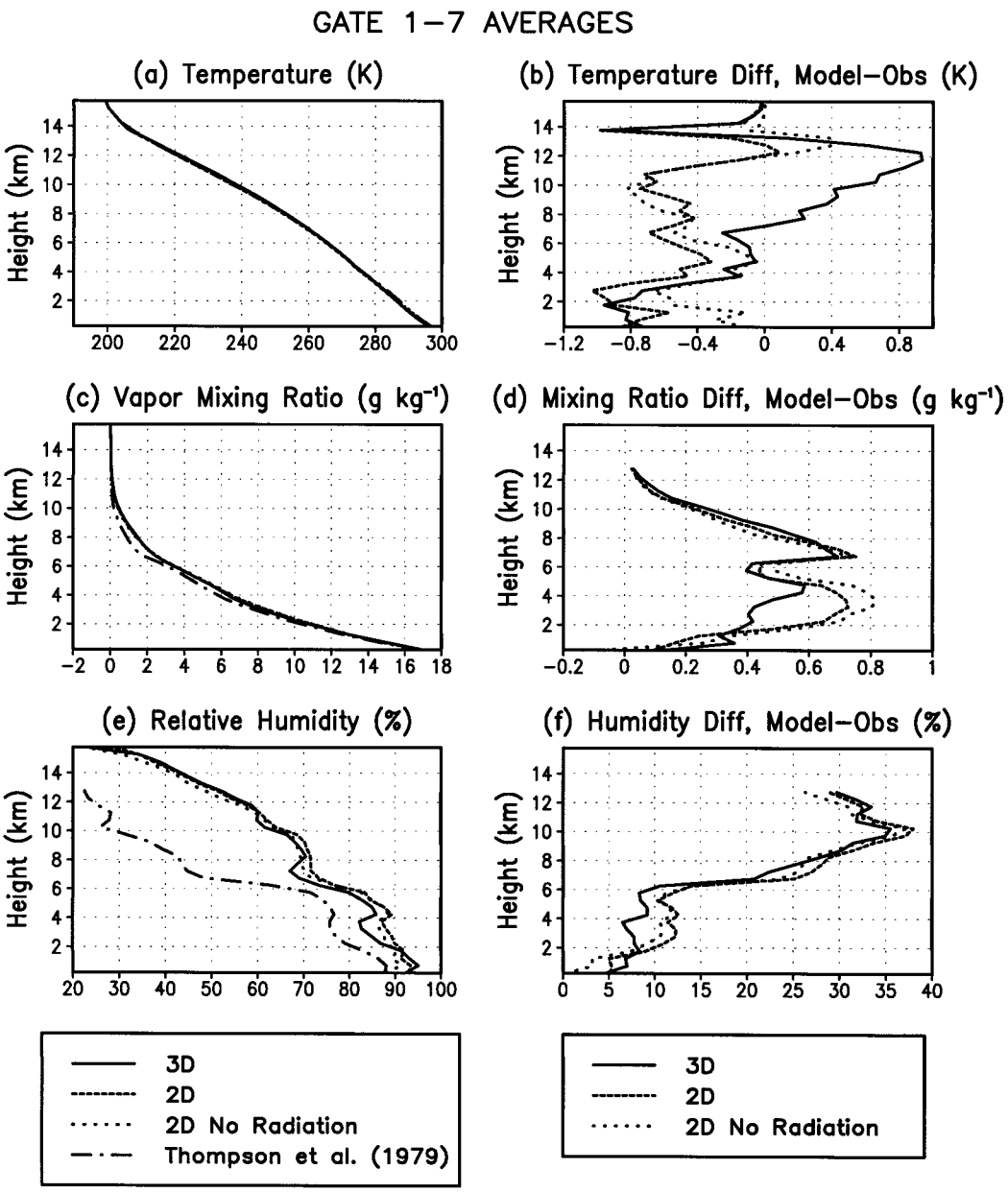

FIG. 6. Averages over GATE phases 1–7 for (a) temperature, (c) vapor mixing ratio, and (e) relative humidity (liquid). Average differences over GATE phases 1–7 between observations and model integrations for (b) temperature, (d) vapor mixing ratio, and (f) relative humidity (liquid).

as produced in cloud-system models will require further analysis to address this issue.

Surface fluxes are shown in Fig. 9. During the preconvective period, sensible-heat fluxes increase as the temperatures in the lowest model layers decrease (not shown), except for 2D No Radiation. Moisture fluxes decrease prior to the development of deep convection, with lower-atmosphere mixing ratios increasing as surface evaporation proceeds without appreciable mechanisms operating to remove water vapor. When deep convection develops, both sensible- and latent-heat fluxes increase, at least initially. These enhanced fluxes can be ascribed to two mechanisms. 1) Convection changes the temperature and humidity fields in the lower atmosphere, altering the surface–atmosphere differences in these fields. 2) Enhanced horizontal winds associated with convection in the lower atmosphere increase fluxes. As deep convection dissipates in the later stages of the integration, fluxes generally decrease.

The surface fluxes reported by Thompson et al. (1979) are also shown in Fig. 9. Although surface temperatures for the model integrations are selected to produce the

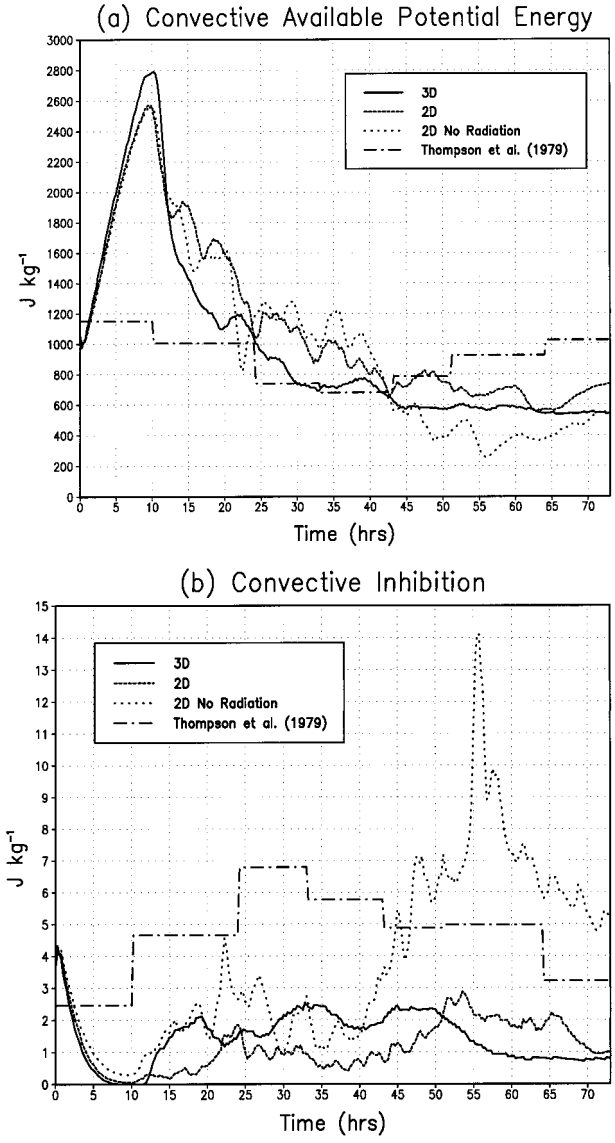

FIG. 7. Domain-averaged (a) convective available potential energy and (b) convective inhibition. Thompson et al. (1979) observations are phase averaged.

observed sensible-heat fluxes with observed atmospheric temperature profiles, the model fluxes differ from observed fluxes. These differences are results of the model's domain-averaged state developing somewhat differently from the observed state (Fig. 5) and the generation of significant small-scale structure in near-surface fields around convective elements. The observed surface moisture fluxes are generally larger than the modeled fluxes, while observed sensible-heat fluxes are smaller. This result is consistent with the general tendency for modeled lower-atmosphere temperatures to be cooler than observed (increasing modeled surface fluxes), while modeled lower-atmosphere mixing ratios are more variable compared to observations, often higher than observed during early phases when modeled surface moisture fluxes are below observed (Fig. 5).

4. Microphysics and radiation

Domain-averaged microphysical properties for the 3D integration are shown in Fig. 10. Cloud liquid (Fig. 10a) is greatest during intense deep convective events. Its presence lessens considerably after 45 h or so during the mesoscale stratiform period. By contrast, cloud ice (Fig. 10b) shows a strong signature of the mesoscale stratiform circulation, which dominates the last two-thirds of the integration. The steadier nature of the stratiform circulation, relative to more episodic deep convection, is evident in these fields. The rain distribution (Fig. 10c) carries a strong signature of deep convective events. Under occasional circumstances where convection is associated with large vertical velocities, some rain can be advected to heights where temperatures are quite low. In the early stages of the convective system, snow often overlies rain, but snow persists longer into the integration (Fig. 10d).

Cloud liquid and cloud ice have magnitudes similar to those reported by Grabowski et al. (1996b), except for the large cloud-ice maxima at the onset of convection. The vertical distribution of ice is quite different from Grabowski et al. (1996b), however; their maximum concentrations are around 6 km. They note the marked dependence of this vertical structure on the details of the microphysical parameterization. Fu et al. (1995), Chin et al. (1995), and Guichard et al. (1996) also model the microphysical characteristics of deep convection in GATE. Two-dimensional models are employed in all of these studies. Fu et al.'s (1995) and Guichard et al.'s (1996) ice distributions have their stratiform maxima from 8 to 12 km with values exceeding 0.1 g kg^{-1} where stratiform development is greatest. Chin et al.'s (1995) results show stratiform ice maxima around 11 km with concentrations between 0.5 and 1 g kg^{-1}. Figure 10c exhibits higher rain maxima than Grabowski et al. (1996b).

Only limited microphysical observations are available for comparison with Fig. 10, and these generally do not permit direct comparison. Jorgensen and LeMone (1989) report cloud water contents in oceanic convective clouds (for hurricanes and the Taiwan area) of 0.5–1 g m^{-3}. Their measurements are from updraft cores and should be appreciably larger than the domain averages shown in Fig. 10. Figure 2b shows that cores (areas with upward motions greater than 3 m s^{-1}) occupy a limited fraction of the horizontal domain. Restricting liquid to cores with areas based in Fig. 2b suggests liquid concentrations in the cores broadly consistent with those in Jorgensen and LeMone (1989).

Regarding observations of ice and snow, Griffith et al. (1980) used a one-dimensional particle spectrometer to measure ice particles larger than 20 μm in GATE ''dense cirrus outflow.'' Their peak observations were

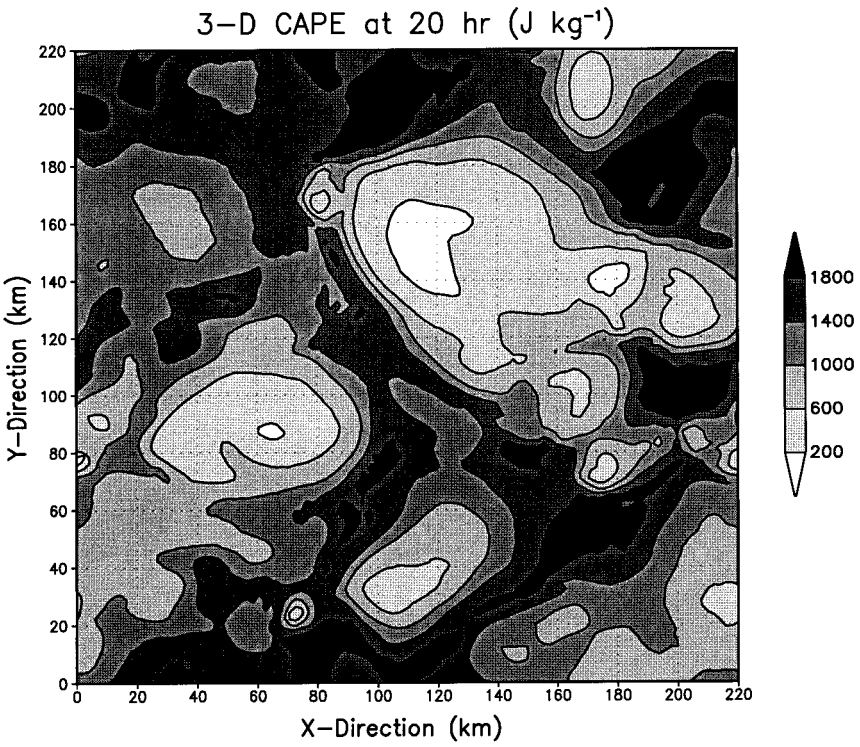

FIG. 8. The 3D convective available potential energy at 20 h.

about 0.3 g m^{-3}. Their experimental uncertainty, arising mostly because of the need to assume an ice-particle shape to calculate ice content from the spectrometer data, was 40%. For a stratiform anvil observed during the GARP Winter Monsoon Experiment near Borneo, Churchill and Houze (1984) used radar to estimate precipitating ice (snow, in the model context) and budget considerations to estimate cloud ice. Their peak sum (total ice content) was around 1 g m^{-3}. The values for snow and cloud ice in Figs. 10b and 10d are consistent with the constraints provided by these measurements, which were rather weak given experimental uncertainty and measurement environments differing from those in the model.

Figure 11 summarizes the condensate distributions over the entire period of integration. Cloud ice is a significant component. Particularly striking in Fig. 11 is the dependence of the ratio of condensate to vapor on the dimensionality and presence or absence of radiation. Grabowski et al. (1996b) found a maximum value for this ratio of only 0.25 at around 13 km in their two-dimensional calculations. Microphysics appears to be a property that is strongly dependent on details of model formulation. Variations in the treatment of cloud-ice sedimentation could be an especially important detail.

Surface precipitation as a function of time is illustrated in Fig. 12a. Consistent with CAPE in Fig. 7a, modeled precipitation is too low during GATE phase 1 before convection develops and too high during the early stages of deep convection. Precipitation is also low during many of the later stages. Both observed and modeled precipitation are largest during the phases dominated by deep convection, although precipitation continues into the phases dominated by stratiform precipitation. Modeled precipitation is quite noisy; only phase averages are available in Thompson et al. (1979). Over the entire length of integration, precipitation totals about 2.8 cm for both two-dimensional integrations and about 3.0 cm for 3D; Thompson et al.'s (1979) estimate is about 4.2 cm. The distribution of surface precipitation (total for entire length of integration) is shown in Fig. 12b. (Unlike other figures, Fig. 12b is mapped for the entire domain over which the model moves with the mean vertically averaged wind. The precipitation in Fig. 12a is calculated with respect to the untranslated domain.) In the sheared environment of the mean GATE sounding, convection tends to have roughly a linear organization with embedded maxima.

Especially during the phases dominated by mesoscale stratiform circulations, radiative forcing is quite large (Fig. 13). Significant longwave cooling occurs at cloud top, with warming at the base of the stratiform circulation. Warming is very pronounced when there is relatively little liquid between the surface and the base of the stratiform circulation (early and late stages of integration). Cloud-top cooling is most pronounced when condensate concentrations are highest near the top of the cloud, also during early and late stages of the integration. The distributions of condensate and radiative

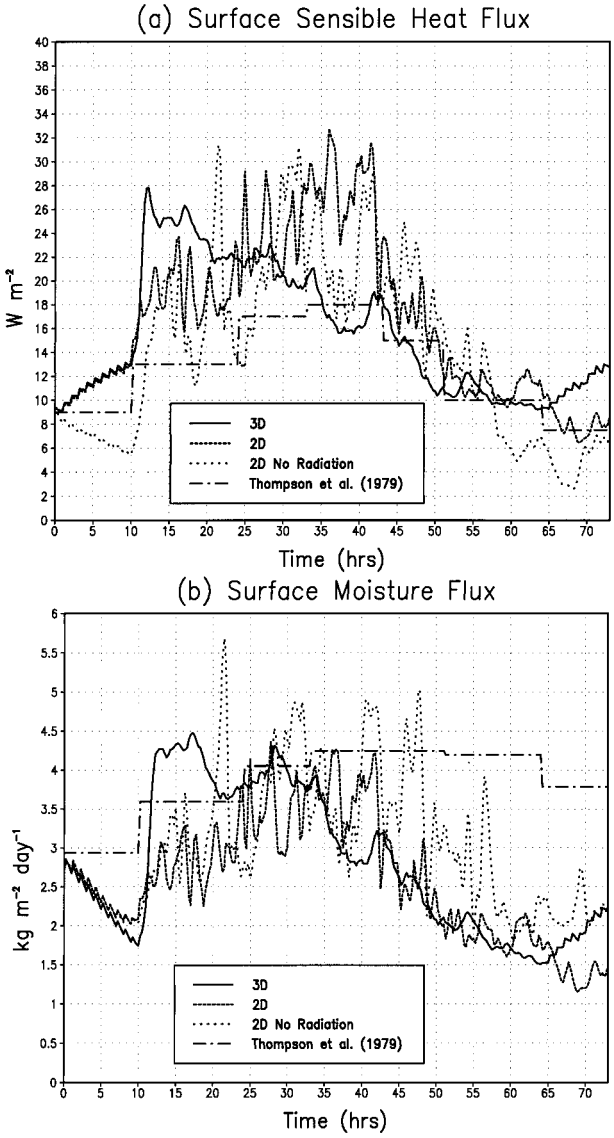

FIG. 9. Domain-averaged surface (a) sensible-heat flux and (b) moisture flux. Thompson et al. (1979) observations are phase averaged.

heating and cooling are intimately linked, as Fig. 14 shows. (As suggested by Fig. 10, the deep convective towers in Fig. 14 consist mostly of snow and rain, with cloud water accounting for very roughly about one-third of the total condensate at most heights in the towers. The stratiform canopy is dominated by cloud ice.) Vertical gradients in radiative heating and cooling of 30 K day^{-1} over just a few kilometers are common. Radiative heating and cooling here substantially exceed those of Grabowski et al. (1996b), whose maximum magnitudes, averaged over their 7-day integration period, do not exceed 2 K day^{-1}.

The strong vertical gradients in radiative heating and cooling influence the evolution of other aspects of the convective system. To illustrate some of these differences, the 2D and 2D No Radiation integrations can be compared (Figs. 15b,c). As the system moves from convective domination to stratiform domination (35–50 h), the integration with radiation has more condensate at heights around 10 km. Enhanced condensate due to radiation is particularly apparent in the ratio of condensate to vapor; the maximum value of this ratio is nearly twice as large in 2D as in 2D No Radiation (Fig. 11b).

The effect of radiation on CAPE varies with time during the integration (Fig. 7a). The two-dimensional integration with radiation has more CAPE during the early parts of the convectively dominated stage and during the stratiform stage. The integration without radiation has more CAPE during the latter part of the convectively dominated stage, as transition to stratiform domination begins. Usually, radiative cooling destabilizes, thereby increasing CAPE, but the CAPE can decrease when radiative heating at the base of the stratiform circulation results in temperature increases there, stabilizing the lapse rate beneath the radiative heating zone. CIN is consistently greater without radiation (Fig. 7b). Both lower-tropospheric lapse rate and mixing ratio determine CIN. Some of the largest differences between CIN in integrations with and without radiation occur when surface mixing ratios differ (Figs. 5l–n).

Surface sensible-heat fluxes in the two-dimensional integrations are often higher with radiation (Fig. 9a). Averaged over the entire integration, the surface sensible-heat flux is 16.8 W m^{-2} in 2D and 14.4 W m^{-2} in 2D No Radiation. The higher fluxes result from lower atmospheric temperatures in the presence of radiative cooling near the surface (Figs. 6b, 13). For fixed (warmer) surface temperatures, the surface fluxes are higher with cooler atmospheric temperatures, if the wind speeds are comparable. Conversely, surface moisture fluxes are often higher without radiation. Subgrid mixing depends on Richardson number, and radiative cooling is often greater immediately above the surface than slightly higher (Fig. 13b). As a result, less vapor transport by subgrid mixing occurs internally in the atmosphere with radiation, and vapor mixing ratios in the lowest 0.5 km are somewhat higher (Fig. 6d). The smaller vapor mixing-ratio difference between the surface and overlying atmosphere results in lower surface moisture fluxes. Averaged over the entire integration, the surface moisture flux is 2.60 kg (water) m^{-2} day^{-1} in 2D and 3.04 kg (water) m^{-2} day^{-1} in 2D No Radiation.

5. Impact of third dimension

Temperatures in the three-dimensional integration are closer to observed temperatures than those in the two-dimensional integrations from about 4 to 9 km; 3D and 2D are similar below 4 km (Fig. 6b). Mixing ratios in the three-dimensional integration are closer to observed mixing ratios than those in the two-dimensional integrations between 1 and 6 km; all three integrations have

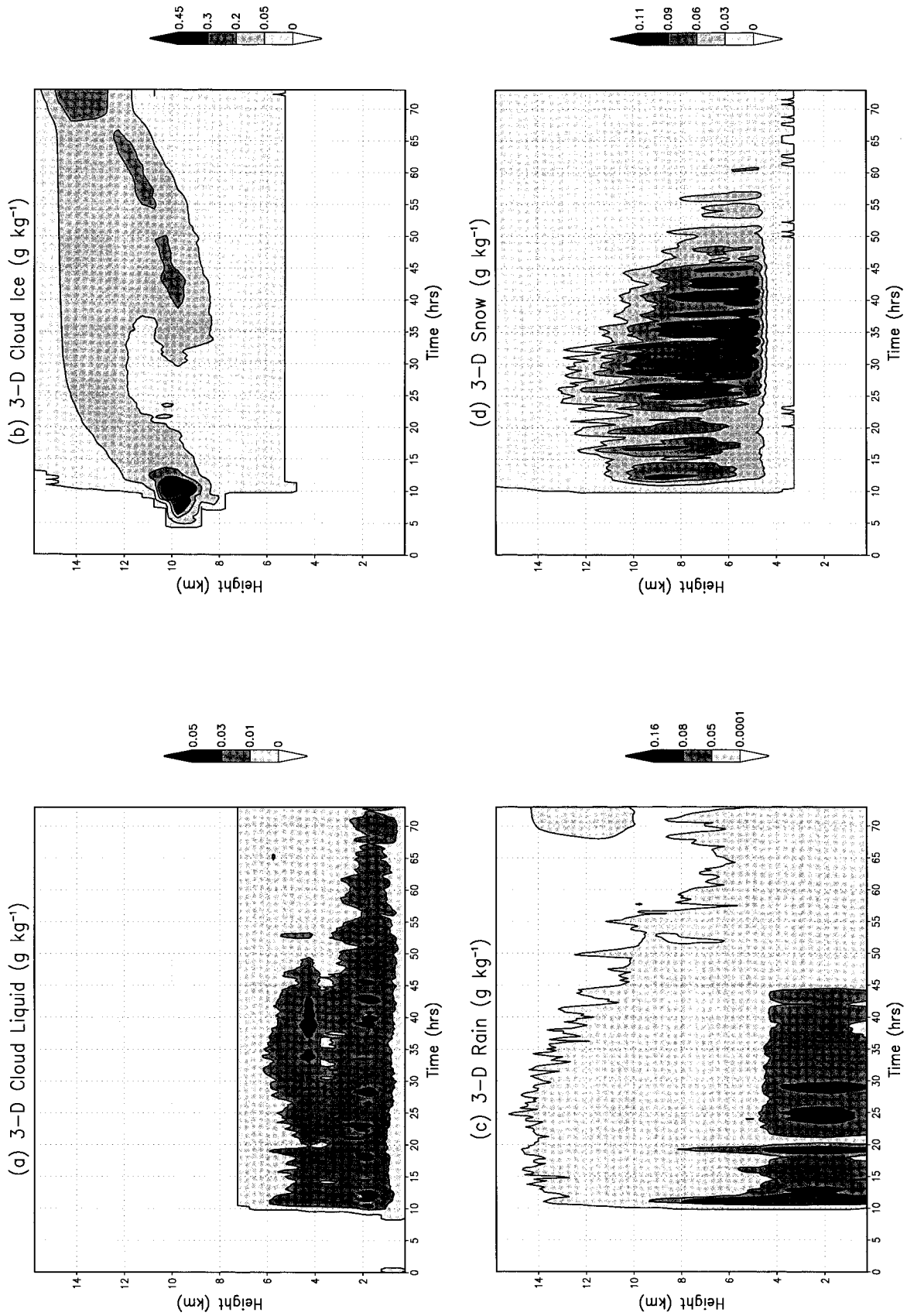

FIG. 10. The 3D horizontally averaged (a) cloud liquid, (b) cloud ice, (c) rain, and (d) snow. Mixing-ratio range from (a) 0 to 0.06, (b) 0 to 0.68, (c) 0 to 0.17, and (d) 0 to 0.14 g kg^{-1}.

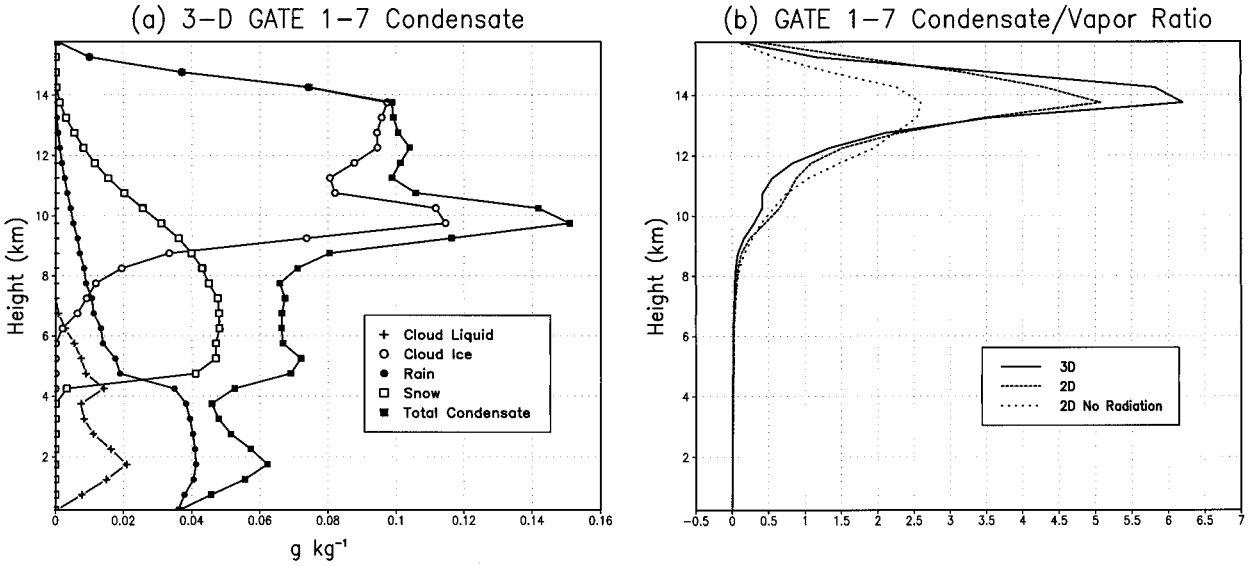

FIG. 11. Averages over GATE phases 1–7 for (a) condensate components and (b) ratio of condensate to vapor.

fairly similar mixing ratios elsewhere (Fig. 6d). The third dimension has no appreciable impact on the inability of the model to capture the sharp decline observed in relative humidity above 6 km (Fig. 6e).

The most significant impact of the third dimension on cloud-system properties averaged over a wave phase or longer is on the mesoscale stratiform circulation. Radiative heating of the base of the stratiform region is greater in 3D than 2D (Fig. 13). Small-scale convective bubbles develop in response to destabilizing radiation, but to an appreciable extent only in 3D. Evidence for these bubbles can be seen in Figs. 4f and 4g, where strong cooling is evident at the stratiform base and strong warming at its top in the Q_T profile for 3D. Most of the contribution to these features in Q_T is from the convergence of the eddy potential-temperature flux, the last term on the right in (5). These eddy motions oppose the destabilizing radiation in the stratiform region but are not sufficiently large to compensate it completely. (Further, the maximum dynamic warming is at a slightly lower height than the maximum radiative cooling.) The uncompensated radiative heating at the base of the stratiform anvil leads to temperatures warmer in 3D than observations or any of the other integrations between 6 and 12 km during phases 6 and 7. Temperatures in 2D exhibit some of the same behavior as those in 3D during these phases, but to a lesser extent.

The intense dynamics in the 3D stratiform region displace condensate upward (Figs. 15a,b). The maximum condensate concentration during the stratiform period is over 2 km higher in 3D than 2D, indicating a stronger feedback between radiation and dynamics in 3D. The maximum ratio of condensate to vapor is approximately 25% larger in 3D than 2D (Fig. 11b).

From phase 2 onward, CAPE is usually smaller in the three-dimensional integration (Fig. 7a). For phases 2–5, which are dominated by deep convection, CIN is usually larger in 3D (Fig. 7b). Deep convection is evidently more easily maintained in 3D, persisting with less CAPE and overcoming greater CIN after initial development.

Another important difference between the 3D and 2D integrations is in the degree of temporal variability. The 2D integration exhibits much more variability, as measured by surface precipitation (Fig. 12a); potential-temperature-flux convergence, the last term on the right in (5) (Fig. 16); moisture-flux convergence, the last term on the right in (6) (Fig. 17); Q_T (Fig. 18); or Q_Q (Fig. 19). Particularly evident from about 50 h onward in Fig. 16a is pronounced heat-flux convergence at the top of the stratiform region with heat-flux divergence at its base. As discussed above, this feature is largely absent in 2D (Fig. 16b). Since cumulus parameterizations for large-scale models often concern themselves with interactions between large-scale flows and convection on timescales of less than an hour, the different temporal behaviors in the 3D and 2D integrations may be an important distinction for using cloud-system models to evaluate scale interactions incorporated in these parameterizations (especially for nonsquall cloud clusters such as are depicted in the horizontal cross sections from 3D in Figs. 2b, 2c, and 8).

Jabouille et al. (1996) note that correlations between wind, temperature, and humidity at convective scales can increase surface fluxes from values in an undisturbed flow with similar mean properties. They estimate these increases at around 5% for sensible-heat fluxes and 1% for moisture fluxes in the equatorial west Pacific. Esbensen and McPhaden (1996) estimate these increases to be up to 26% and 14%, respectively. In the 3D (2D, 2D No Radiation) integration, the increases are 47% (31%, 69%) for sensible-heat fluxes, and 43% (26%,

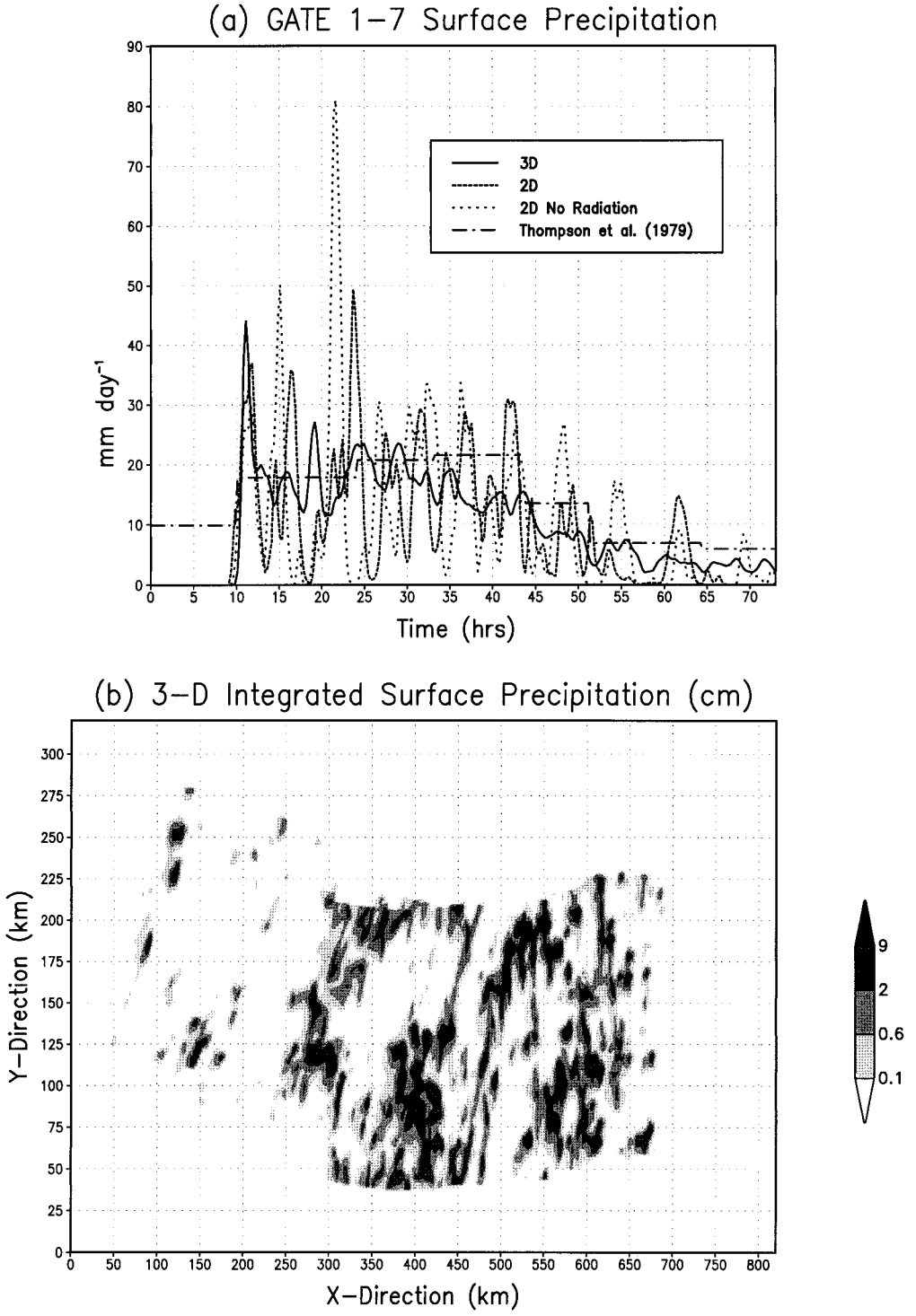

FIG. 12. (a) Domain-averaged surface precipitation rate. Thompson et al. (1979) observations are phase averaged. (b) Total precipitation from GATE phases 1–7. Model domain moves with vertical mean wind to produce precipitation distribution.

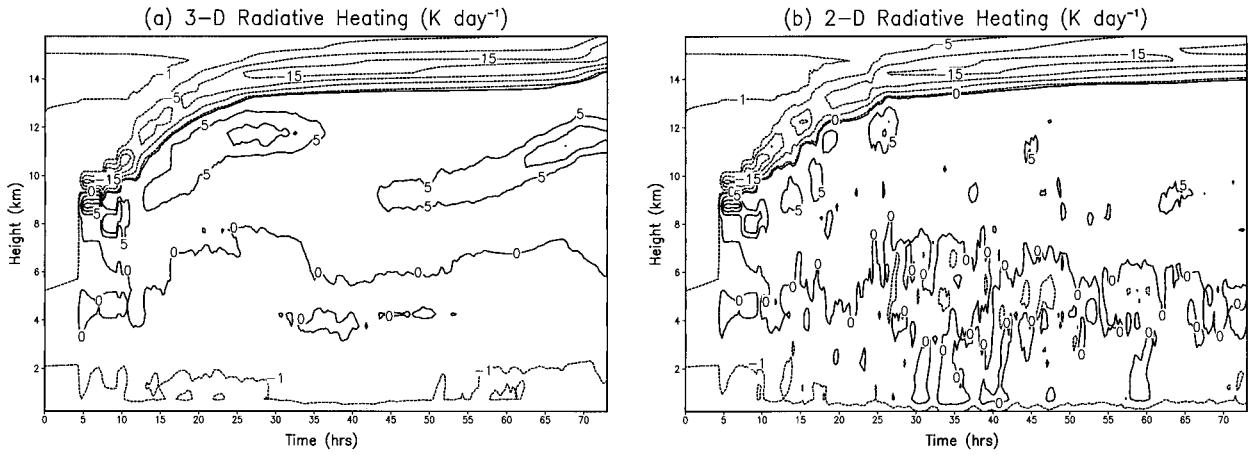

FIG. 13. Horizontally averaged radiative heating for (a) 3D and (b) 2D integrations. Contour levels are −15, −10, −5, −1, 0, 5, 10 K day^{-1}. Negative contours are dashed.

42%) for moisture fluxes, respectively. (The model results are averages over the entire integration.) The finer resolution in the model results may explain the larger enhancements versus observations. The 3D integrations permit the development of more structure, consistent with the larger 3D enhancements relative to 2D. The larger enhancement in 2D No Radiation than 2D is particularly noticeable around 40–55 h (not shown).

6. Concluding remarks

Several features of the integrations of the cloud-system model are especially noteworthy. The modeled system is dominated by deep convection in its early stages and by stratiform circulations in its late stages. Both deep convection and the stratiform circulation are important during intermediate stages. This behavior can

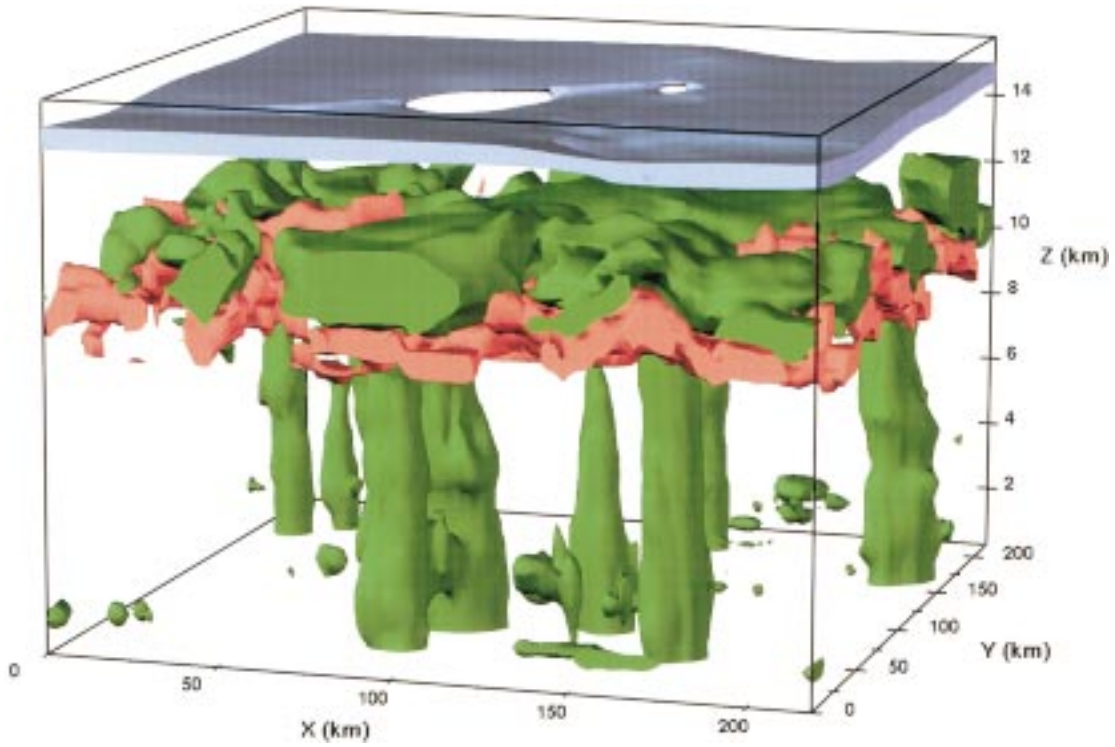

FIG. 14. Three-dimensional distribution of total condensate and its relationship to radiative heating and cooling at 53.75 h. Colored surfaces enclose volumes whose condensate, heating, or cooling magnitudes exceed 0.20 g kg^{-1}, 12 K day^{-1}, and −14 K day^{-1}, respectively.

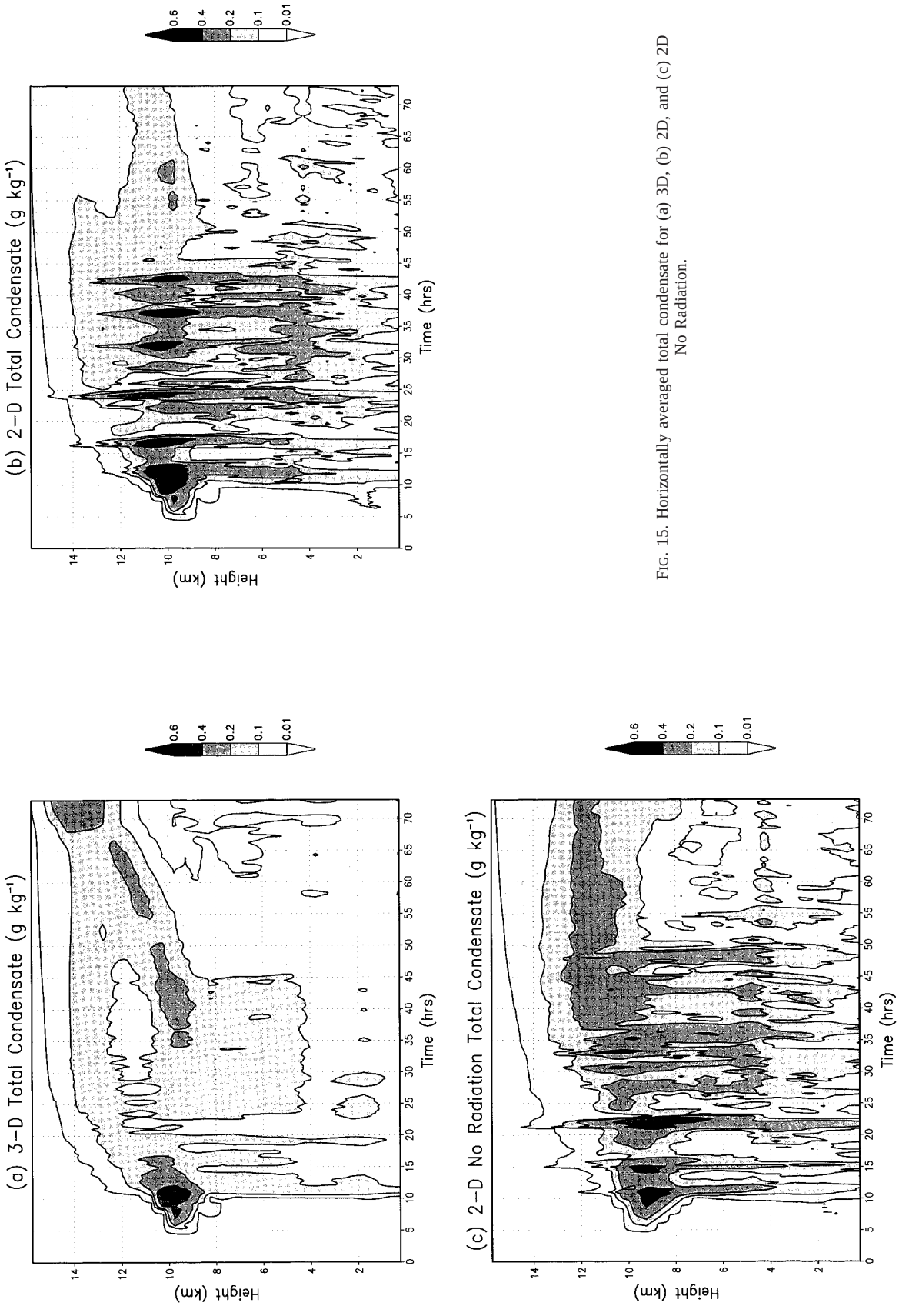

FIG. 15. Horizontally averaged total condensate for (a) 3D, (b) 2D, and (c) 2D No Radiation.

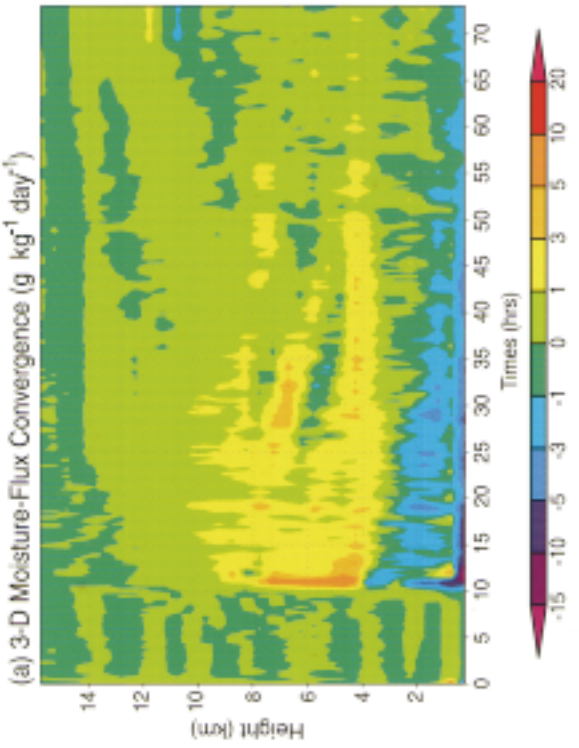

FIG. 17. Moisture-flux convergence $-(1/\overline{\rho})(\overline{\rho w' q'})/\partial z$ for (a) 3D and (b) 2D integrations.

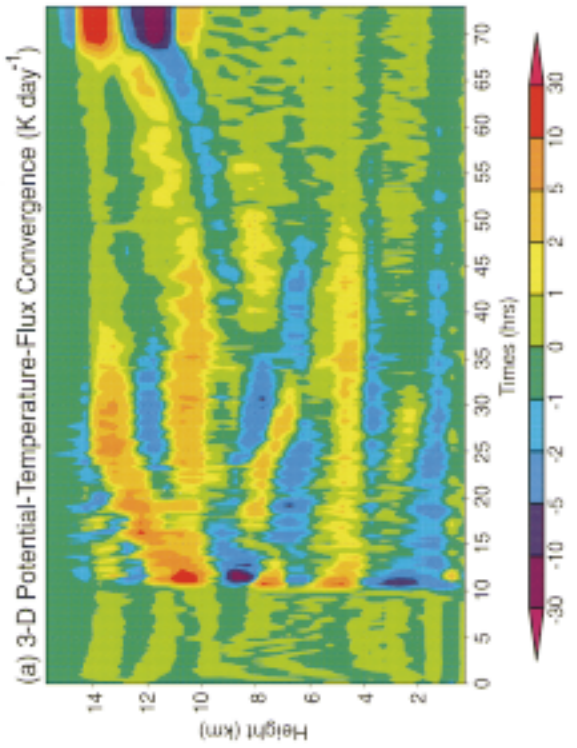

FIG. 16. Potential-temperature-flux convergence $-(1/\overline{\rho\pi})(\overline{\rho w'\theta'})/\partial z$ for (a) 3D and (b) 2D integrations.

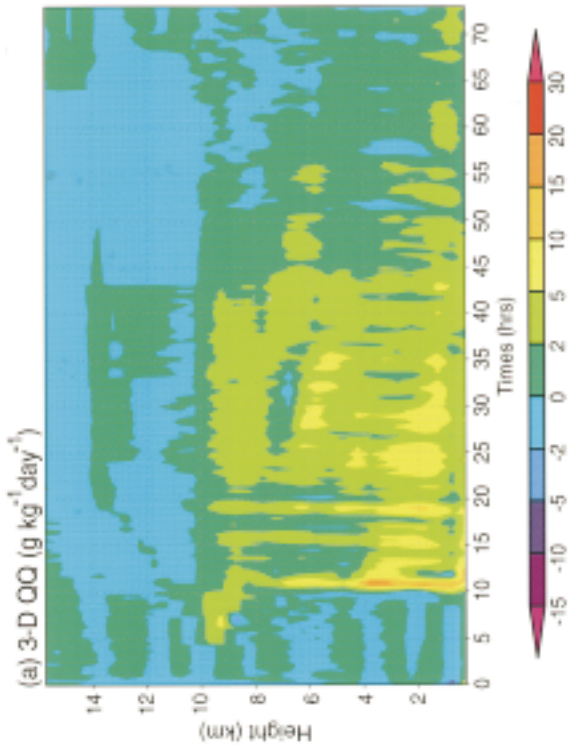

FIG. 18. Thermal forcing Q_T for (a) 3D and (b) 2D integrations.

FIG. 19. Moisture forcing Q_Q for (a) 3D and (b) 2D integrations.

be seen by examining the condensate patterns in Fig. 10. The nature of the convective system in the present integrations is associated closely with the time evolution of the large-scale forcing, with deep convection associated most closely with periods when the middle troposphere is destabilized (Fig. 1a). Note here that ''large scale'' simply defines an averaging operation. It does *not* in any way characterize the motions that compose the average; that is, convective motions may contribute substantially to this average. This average is extremely useful, since it is resolved by models with the resolution of general circulation models and (to an appreciable degree) by atmospheric observing systems.

Leary and Houze (1980) observe a GATE convective system to undergo a similar evolution. However, the lifetime of their system is about 24 h, in contrast to the 3-day integration here. Leary and Houze's (1980) composite system is drawn mostly from 5 September 1974. Thompson et al. (1979) indicate their system was in phase 2 for 12 h (6 h on 5 September), phase 3 for 12 h, and phase 4 for 15 h (6 h on 5 September). Phases 3 and 4 are both longer than the composite values used in these integrations. The integration phases corresponding to those on 5 September extend from approximately 16 to 36 h. There is some evidence in these integrations of individual systems evolving like that of Leary and Houze (1980), even while they are parts of the more general pattern associated with large-scale forcing. Around 20 h in 3D, surface precipitation increases (Fig. 12a) and maxima in cloud liquid and rain in the lower part of convective towers develop (Figs. 10a,c). Stratiform cloud ice is then at a minimum (Fig. 10b), corresponding to the deep convective stage of Leary and Houze (1980). At 25–30 h, significant snow develops (Figs. 10d), and cloud ice in the stratiform region increases, corresponding to Leary and Houze's (1980) stage with both convective and stratiform activity. At 40 h, rain and snow associated with deep convection have decreased, but a maximum develops in cloud ice, corresponding to Leary and Houze's (1980) stratiform stage. The absence of a diurnal radiation cycle in these composite easterly wave integrations probably alters the intensity and duration of these individual embedded cycles.

Although cumulus parameterizations for large-scale models relate the intensity of convection to large-scale properties in a variety of ways, the nature of the subgrid disturbances that initiate convection is not among these properties. Further, the design of cloud-system model experiments for parameterization evaluation assumes that properties averaged over the large scale are closely linked to the properties of convection. The results obtained here are broadly in support of this approach but do suggest limits, especially in the early stages of convection. In these integrations, the onset of convection is delayed relative to observations, resulting in excessive CAPE buildup, followed by convection of too great intensity. Apparent heat sources and moisture sinks, which are products of parameterizations to be evaluated by cloud-system models, clearly manifest this behavior. Dependence on the details of initialization is indicated. This dependence requires further study.

A striking result from these integrations is the difference in temporal variability, even over the entire domain, between the two- and three-dimensional versions of the cloud-system model. Larger variability in the two-dimensional integrations is probably partly related to the different behavior of the CAPE and CIN in two and three dimensions. Most of the fields associated with the convective ensemble show more variability in two dimensions. The three-dimensional integration has more grid points over which motions may be realized, so some of the reduced variability in the three-dimensional integration may reflect sampling from a larger set of grid columns. The restriction of motions to a plane in the two-dimensional integrations may also be important, since the possible forms of organization of motions are limited. Some behaviors, such as the low CIN in the two-dimensional integrations with radiation, could be results of this limitation. Some inferences regarding the relative roles of these distinctions between two- and three-dimensions could be drawn by comparing ensemble integrations under varying initial perturbations in two dimensions with a three-dimensional integration.

Another prominent result of these integrations is the strong interaction between radiation and the dynamics of the mesoscale stratiform circulation in the three-dimensional integration. The possibility of an equilibrium in which large radiative heating and cooling are balanced by small-scale convective bubbles in the stratiform clouds is suggested. The model results remain somewhat inconclusive due to several model numerical and physical issues. The dynamic heating and cooling do not fully balance the radiative cooling and heating, as indicated by temperature trends relative to observations in the stratiform region.

Other than initialization details, model issues that require further study include 1) use of periodic lateral boundary conditions, (2) sedimentation of cloud ice, (3) vertical and horizontal resolution in the mesoscale stratiform region, and (4) radiative properties of ice. Periodic boundary conditions do not permit ice flowing out of the model domain to leave it; rather, it simply appears at the opposite boundary. Excessive ice concentrations, that exaggerate ice-radiative feedbacks, could result. Cloud ice in these integrations does not settle, despite experimental evidence that ice at concentrations below that at which autoconversion to snow begins does settle (Petch et al. 1997; Heymsfield and Donner 1990; Cotton et al. 1982). Neglecting this mechanism could also lead to excessive ice contents. The failure of the cloud-system model to produce observed decreases with height in middle-troposphere relative humidities strongly suggests inadequate moisture removal, and boundary conditions and ice sedimentation are both plausible culprits.

APPENDIX
Symbols and Units

Symbol	Description	Units
c_p	Specific heat at constant pressure	J kg^{-1} K^{-1}
g	Gravity constant	m s^{-2}
p	Pressure	Pa
p_0	Reference pressure	Pa
R_d	Gas constant for dry air	J kg^{-1} K^{-1}
q	Water vapor mixing ratio	kg (water) kg^{-1}
s	Dry static energy	J kg^{-1}
t	Time	s
w	Vertical velocity	m s^{-1}
z	Height	m
z_0	Height above which sponge applied	m
L_1	Latent heat of vaporization	J kg (water)$^{-1}$
L_2	$-L_1$	J kg (water)$^{-1}$
L_3	Latent heat of sublimation	J kg (water)$^{-1}$
L_4	$-L_3$	J kg (water)$^{-1}$
L_5	Latent heat of fusion	J kg (water)$^{-1}$
L_6	$-L_5$	J kg (water)$^{-1}$
T	Temperature	K
Q_Q	Model large-scale moisture forcing	kg (water) kg^{-1} s^{-1}
Q_T	Model large-scale thermal forcing	K s^{-1}
Q_1	Apparent heat source	J kg^{-1} s^{-1}
Q_2	Apparent moisture sink	J kg^{-1} s^{-1}
κ_0	Constant used to calculate sponge strength	m^{-1} s^{-1}
π	Reciprocal Exner function	dimensionless
ρ	Density	kg m^{-3}
γ_1	Condensation rate	kg (water) kg^{-1} s^{-1}
γ_2	Evaporation rate	kg (water) kg^{-1} s^{-1}
γ_3	Desposition rate	kg (water) kg^{-1} s^{-1}
γ_4	Sublimation rate	kg (water) kg^{-1} s^{-1}
γ_5	Freezing rate	kg (water) kg^{-1} s^{-1}
γ_6	Melting rate	kg (water) kg^{-1} s^{-1}
θ	Potential temperature	K
$\partial_{LS}\overline{q}$	Large-scale forcing for vapor mixing ratio	kg (water) kg^{-1} s^{-1}
$\partial_{LS}\overline{\theta}$	Large-scale forcing for potential temperature	K s^{-1}

$\overline{(\ )}$ refers to a large-scale horizontal average (with respect to field observations) and to an average over horizontal domain (with respect to the model). $(\ )'$ refers to a departure from the horizontal average.

Higher resolution in the stratiform region could enhance the model's ability to respond dynamically to radiatively generated instabilities and lead to more complete compensation of radiation. The present formulation of the cloud-system model does not distinguish between liquid and ice for radiation purposes, and further development is required to elucidate the role of ice properties in radiation and associated feedbacks. These cloud-ice issues are largely unresolved due to limited observations of ice content; presently available observations are not inconsistent with the results of these integrations but are too rudimentary to instill much confidence in them either. Since stratiform circulations can exert large magnitudes of both shortwave and longwave forcing, these issues may be important for climate. If heat fluxes associated with convective bubbles in the stratiform region can compensate large radiative heating and cooling, much larger ice contents (and magnitudes of cloud forcing) are possible than in the absence of a mechanism to compensate.

These cloud-system-model integrations hold much promise as tools for studying the basic behavior of tropical convection and its impact on large-scale flow and climate. The three-dimensional integrations yield a great deal of structure, some of which poses challenges to the general approach of formulating cumulus parameterizations in terms of large-scale variables only. Large variations in CAPE at scales well below those typically resolved in large-scale models are an example. Further development of the cloud-system models regarding microphysics, boundary conditions, and initialization will be required to improve these models as tools for studying interactions among clouds, radiation, convection, and climate.

Acknowledgments. GATE thermodynamic profiles and diagnosed forcing were provided by S. Payne (Naval Environmental Prediction Research Facility). Discussions with Kuan-Man Xu (Colorado State University) on integration design and interpretation of the role of the third spatial dimension were helpful. John Sheldon (GFDL) assisted with the three-dimensional rendering of the cloud system in Fig. 14. Aspects of this research related to convective processes in the atmo-

spheric general circulation were supported by NASA Langley (CERES) Grant 97-1239. Comments on the study by C. Andronache and V. Balaji were appreciated.

REFERENCES

Arakawa, A., and W. H. Schubert, 1974: Interaction of a cumulus cloud ensemble with the large-scale environment, Part 1. *J. Atmos. Sci.,* **31,** 674–701.

Chin, H.-N. S., Q. Fu, M. M. Bradley, and C. R. Molenkamp, 1995: Modeling of a tropical squall line in two dimensions: Sensitivity to radiation and comparison with a midlatitude case. *J. Atmos. Sci.,* **52,** 3172–3193.

Churchill, D. D., and R. A. Houze Jr., 1984: Mesoscale updraft magnitude and cloud-ice content deduced from the ice budget of the stratiform region of a tropical cloud cluster. *J. Atmos. Sci.,* **41,** 1717–1725.

Cotton, W. R., M. A. Stephens, T. Nehrkorn, and G. J. Tripoli, 1982: The Colorado State University three-dimensional cloud/mesoscale model-1982. Part II. An ice phase parameterization. *J. Rech. Atmos.,* **16,** 295–320.

Donner, L., 1993: A cumulus parameterization including mass fluxes, vertical momentum dynamics, and mesoscale effects. *J. Atmos. Sci.,* **50,** 889–906.

——, 1996: Conditional and convective instability. *Encyclopedia of Weather and Climate,* S. H. Schneider, Ed., Vol. 1, Oxford University Press, 186–191.

——, H. L. Kuo, and E. J. Pitcher, 1982: The significance of thermodynamic forcing by cumulus convection in a general circulation model. *J. Atmos. Sci.,* **39,** 2159–2181.

Dudhia, J., and M. W. Moncrieff, 1987: A numerical simulation of quasi-stationary tropical convective bands. *Quart. J. Roy. Meteor. Soc.,* **113,** 929–967.

Emanuel, K. A., 1994: *Atmospheric Convection.* Oxford University Press, 580 pp.

Esbensen, S. K., and M. J. McPhaden, 1996: Enhancement of tropical ocean evaporation and sensible heat flux by atmospheric mesoscale systems. *J. Climate,* **9,** 2307–2325.

Fritsch, J. M., and C. F. Chappell, 1980: Numerical prediction of convectively driven mesoscale pressure systems. Part I: Convective parameterization. *J. Atmos. Sci.,* **37,** 1722–1733.

Fu, Q., S. K. Krueger, and K.-N. Liou, 1995: Interactions of radiation and convection in simulated tropical cloud clusters. *J. Atmos. Sci.,* **52,** 1310–1328.

Golding, B. W., 1993: A numerical investigation of tropical island thunderstorms. *Mon. Wea. Rev.,* **121,** 1417–1433.

Grabowski, W. W., M. W. Moncrieff, and J. T. Kiehl, 1996a: Long-term behaviour of precipitating tropical cloud systems: A numerical study. *Quart. J. Roy. Meteor. Soc.,* **122,** 1019–1042.

——, X. Wu, and M. W. Moncrieff, 1996b: Cloud-resolving modeling of tropical cloud systems during Phase III of GATE. Part I: Two-dimensional experiments. *J. Atmos. Sci.,* **53,** 3684–3709.

Gregory, D., and M. J. Miller, 1989: A numerical study of the parameterization of deep tropical convection. *Quart. J. Roy. Meteor. Soc.,* **115,** 1209–1241.

Griffith, K. T., S. K. Cox, and R. G. Knollenberg, 1980: Infrared radiative properties of tropical cirrus clouds inferred from aircraft measurements. *J. Atmos. Sci.,* **37,** 1077–1087.

Guichard, F., J.-L. Redelsperger, and J.-P. LaFore, 1996: The behaviour of a cloud ensemble in response to external forcings. *Quart. J. Roy. Meteor. Soc.,* **122,** 1043–1073.

Hack, J. J., 1994: Parameterization of moist convection in the National Center for Atmospheric Research community climate model (CCM2). *J. Geophys. Res.,* **99,** 5551–5568.

Harrison, E. F., P. Minnis, B. R. Barkstrom, V. Ramanathan, R. D. Cess, and G. G. Gibson, 1990: Seasonal variation of cloud radiative forcing derived from the Earth Radiation Budget Experiment. *J. Geophys. Res.,* **95,** 18 687–18 703.

Haywood, J. M., V. Ramaswamy, and L. J. Donner, 1997: A limited-area-model case study of the effects of sub-grid scale variations in relative humidity and cloud upon the direct radiative forcing of sulfate aerosol. *Geophys. Res. Lett.,* **24,** 143–146.

Held, I. M., R. S. Hemler, and V. Ramaswamy, 1993: Radiative–convective equilibrium with explicit two-dimensional moist convection. *J. Atmos. Sci.,* **50,** 3909–3927.

Heymsfield, A. J., and L. J. Donner, 1990: A scheme for parameterizing ice-cloud water content in general circulation models. *J. Atmos. Sci.,* **47,** 1865–1877.

Jabouille, P., J. L. Redelsperger, and J. P. Lafore, 1996: Modification of surface fluxes by atmospheric convection in the TOGA COARE region. *Mon. Wea. Rev.,* **124,** 816–837.

Jorgensen, D. P., and M. A. LeMone, 1989: Vertical velocity characteristics of oceanic convection. *J. Atmos. Sci.,* **46,** 621–640.

Kuo, H.-L., 1974: Further studies of the parameterization of the influence of cumulus convection on large-scale flow. *J. Atmos. Sci.,* **31,** 1232–1240.

Leary, C. A., and R. A. Houze Jr., 1980: The contribution of mesoscale motions to the mass and heat fluxes of an intense tropical convective system. *J. Atmos. Sci.,* **37,** 784–796.

Lelieveld, J., and P. J. Crutzen, 1994: Role of deep convection in the ozone budget of the troposphere. *Science,* **264,** 1759–1761.

Lipps, F. B., and R. S. Hemler, 1986: Numerical simulation of deep tropical convection associated with large-scale convergence. *J. Atmos. Sci.,* **43,** 1796–1816.

——, and ——, 1988: Numerical modeling of a line of towering cumulus on day 226 of GATE. *J. Atmos. Sci.,* **45,** 2428–2444.

Paradis, D., J. P. Lafore, J. L. Redelsperger, and V. Balaji, 1995: African easterly waves and convection. Part I: Linear simulations. *J. Atmos. Sci.,* **52,** 1657–1679.

Petch, J. C., G. C. Craig, and K. P. Shine, 1997: A comparison of two bulk microphysical schemes and their effects on radiative transfer using a single-column model. *Quart. J. Roy. Meteor. Soc.,* **123,** 1561–1580.

Redelsperger, J. L., and G. Sommeria, 1986: Three-dimensional simulation of a convective storm: Sensitivity studies on subgrid parameterization and spatial resolution. *J. Atmos. Sci.,* **43,** 2619–2635.

Slingo, J. M., and Coauthors, 1994: Mean climate and transience in the tropics of the UGAMP GCM: Sensitivity to convective parameterization. *Quart. J. Roy. Meteor. Soc.,* **120,** 881–922.

Soden, B. J., and R. Fu, 1995: A satellite analysis of deep convection, upper-tropospheric humidity, and the greenhouse effect. *J. Climate,* **8,** 2233–2351.

Stenchikov, G., R. Dickerson, K. Pickering, W. Ellis Jr., B. Doddridge, S. Kondragunta, and O. Poulida, 1996: Stratosphere–troposphere exchange in a midlatitude mesoscale convective complex. 2. Numerical simulations. *J. Geophys. Res.,* **101,** 6837–6851.

Sui, C. H., K. M. Lau, W. K. Tao, and J. Simpson, 1994: The tropical water and energy cycles in a cumulus ensemble model. Part. I: Equilibrium climate. *J. Atmos. Sci.,* **51,** 711–728.

Tao, W.-K., and S.-T. Soong, 1986: A study of the response of deep tropical clouds to mesoscale processes: Three-dimensional numerical experiments. *J. Atmos. Sci.,* **43,** 2653–2676.

——, J. Simpson, C.-H. Sui, B. Ferrier, S. Lang, J. Scala, M.-D. Chou, and K. Pickering, 1993: Heating, moisture, and water budgets of tropical and midlatitude squall lines: Comparisons and sensitivity to longwave radiation. *J. Atmos. Sci.,* **50,** 673–690.

Thompson, R. M., S. W. Payne, E. E. Recker, and R. J. Reed, 1979: Structure and properties of synoptic-scale wave disturbances in the intertropical convergence zone of the eastern Atlantic. *J. Atmos. Sci.,* **36,** 53–72.

Xu, K.-M., and S. K. Krueger, 1991: Evaluation of cloudiness parameterization using a cumulus ensemble model. *Mon. Wea. Rev.,* **119,** 342–367.